Division of Solid Mechanics

ISRN LUTFD2/TFHF--01/5097--SE (1-54)

STRUCTURAL OPTIMIZATION OF TRAIN CRASH STRUCTURE

Master's Dissertation by

Anders Larbrant

Supervisors
Mikeal Norman,Bombardier Transportation, Sweden
Mathias Wallin, Div. of Solid Mechanics
Paul Håkansson, Div. of Solid Mechanics
Matti Ristinmaa, Div. of Solid Mechanics

Printed by KFS i Lund AB, Lund, Sweden, 2002.

For information, address:
Division of Solid Mechanics, Lund University, Box 118, SE-221 00 Lund, Sweden.
Homepage: www.solid.lth.se

Acknowledgements

This work was carried out at Bombardier Transportation, Kalmar, Sweden and at the Division of Solid Mechanics, Department of Mechanical Engineering, Lund Institute of Technology, Lund University, Sweden under supervision of Professor Matti Ristinmaa.

I whish to thank Ph.D.-students Mathias Wallin and Paul Håkansson and Professor Matti Ristinmaa for their guidance. I would also like to thank Engineering Research AB for being generous with support and the LS-OPT license.

At Bombardier Transportation, I would like to thank Mikael Norman for interesting and valuable discussions.

Kalmar/Lund, October 2002

Anders Larbrant

Abstract

Crash analysis has been performed for several years at Bombardier Transportation, former Adtranz, Kalmar, Sweden.

Proceeding one step further, the current study is focused on optimization of a front structure during crash-loading conditions. This is the first study within Bombardier Transportation in the area of crash optimization. Therefore the finite element model was kept as simple as possible without loosing relevance of the purpose of the study, i.e. to examine how much weight that can be reduced from the current crash-structure without worsen the crash performance. The analyzed structure was the crash-structure of the regional train Crusaris Regina.

The optimization tool was LS-OPT together with the explicit code of LS-DYNA. Several ways to set up an optimization are offered by LS-OPT and the current study focused on intrusion and acceleration as constraints for the optimization.

Three different approaches were used to define the constraint due to acceleration.

The current thesis only regards optimization of thickness, which is the simplest optimization category. Several simplifications were introduced and therefore the results obtained from the current study cannot be directly transferred to the current design. Instead the results presented shall be compared with the original design i.e. the relative improvements/deterioration's from the optimized design in comparison with design before any optimization analyses were performed.

The analyses have shown that the weight of the structure can be reduced. Due to time-limitations of the license of the software LS-OPT, a total satisfactory solution was not obtained, but the results achieved indicate that a weight reduction of 50 kg. is realistic. It has to be remembered that the crash-structure already, during the development of the Crusaris Regina, has been manually optimized on a trial and error basis, which took approximately one half of a man-year. LS-OPT required approximately two weeks of simulation time to achieve a structure with the same crash-performance but with a weight reduction of approximately 50 kg.

The study also showed that the result of the optimization can be very dependent on how certain constraints are defined, in this case the accelerations. Also, the study showed that the computation time is highly dependent on the number of design variables and the number of iterations LS-OPT is allowed to perform. The number of available processors and LS-DYNA licenses has a major influence on the calculation time.

Including LS-OPT early in the product development of future crash-structures will result in a shorter development time and an optimized design.

1. Notation

X_i	*Material coordinates*
x_i	*Spatial coordinates*
u_i	*Displacement vector*
E_{ij}	*Green-Lagrange strain tensor*
F_{ij}	*Deformation gradient*
L_{ij}	*Spatial velocity gradient*
δ_{ij}	*Kronecker's delta*
W_{ij}	*Spin tensor*
t_i	*Traction vector*
σ_{ij}	*Cauchy stress tensor*
n_j	*Normal vector*
P_{ij}	*First Piola-Kirchhoff stress tensor*
S_{ij}	*Second Piola-Kirchhoff stress tensor*
ε_{ij}	*Small strain tensor*
v_i	*Velocity vector*
$\dot{\sigma}_{ij}$	*Stress rate*
L_{ijkl}	*Isotropic stiffness tensor*
$\overset{o}{\sigma}_{ij}$	*Jaumann stress rate (objective stress rate)*
s_{ij}	*Deviatoric stress*
J_2	*Stress invariant*
F	*Yield function*
K	*Hardening parameter*
$\dot{\lambda}$	*Plastic multiplier*
σ_y	*Yield stress*
H	*Plastic modulus*
G	*Shear modulus*
υ	*Poisson´s ratio*
$\overset{\Delta}{\sigma}_{ij}$	*Truesdell stress rate*

2. Introduction

Bombardier Transportation is a subsidiary company within Bombardier and is the largest supplier of trains in the world with 36 000 employees and production facilities all over the world.

This thesis was performed at the Department of Structural Mechanics at Bombardier Transportation, Kalmar, Sweden where crashworthiness analysis has been performed for about eight years.

In the conventional development cycle, the design is first ensured to withstand certain criteria and then experienced- or intuition-based design changes are usually made to achieve certain goals for instance a lower mass of the design. This procedure is time-consuming and often the demands stated on the design are in conflict with each other, for instance high stiffness and low acceleration levels together with low mass. It is not obvious how a change of a certain design parameter will influence the response and if it will be advantageous to the solution of the problem as a whole. The complexity of the problem grows larger when considering a complex structure together with a highly nonlinear processes such as a crash analysis of a train crash structure. Therefore, more intelligent ways to perform optimization analysis need to be investigated.

The aim with the current study is to investigate whether LS-OPT can be of any use for the future development of new trains within Bombardier Transportation. This thesis is the first step towards the use of special software for optimization of structures exposed to crash loading within Bombardier Transportation. Therefore the model investigated was considered to be as simple as possible but still be relevant enough to the purpose, i.e. optimization of large, complex structures during a highly nonlinear processes, in this case train crashworthiness analysis. The current thesis only regards optimization of thickness, which is the simplest optimization category. Several simplifications were introduced and therefore the results obtained from the current study cannot be directly transferred to the current design. Instead the results presented must be compared with the original design i.e. the relative improvements/deterioration's from the optimized design in comparison with design before any optimization analyses were performed. Therefore, no effort is put into describing the material properties or the true stress-true strain curves for the different materials used. For such data it is referred to the technical report of the crashworthiness analysis of the Crusaris Regina, 3EST 76-857.

In order to obtain accurate results, the understanding of the underlying theories are essential when performing finite element analyses. The theories involved in optimization of crash structures are for instance optimization, contact, plasticity and large deformations. All theories are rather extensive. Therefore, the current study is restricted to the theory of large deformations and hypo-elastoplasticity, which are presented in the following chapter.

3. Nonlinear Finite Element Theory

In linear finite element analysis the deformations and rotations of a continuum are considered as small and the loads applied to the continuum are assumed not to cause any plastic deformations i.e. the response in the structure is considered to be linear elastic. However, performing finite element analysis regarding vehicle crashworthiness where the structure must deform in a controlled manner to lower the accelerations, plastic response, large deformations together with contact must be taken into account. In the current chapter an introduction to nonlinear finite element theory will be presented with respect to large deformation and the nonlinear response in the material i.e. the constitutive law.

3.1 Kinematics – Large Deformations

Displacements of a body under load can be divided into two categories: *deformation and rigid body motion*. When a body is under load, the body may be displaced without having developed any stresses, a rigid body motion. The body may be displaced in such a way that stresses are developed, i.e. a deformation. These two displacements must be separated since only deformations give rise to stresses. This is usually done by comparing the current configuration with a reference configuration. Consider a continuum before an arbitrary load is applied. This state of the continuum is denoted as the *reference configuration*. Each material particle in the continuum can be described by its material coordinates, X_i. After an arbitrary load is applied, the continuum deforms and this state is denoted the *deformed configuration* or the *current configuration*. The coordinates in the deformed configuration, x_i, are described by the material coordinates in the reference configuration and the displacements due to the applied load i.e.:

$$x_i(X_k) = X_i + u_i(X_k, t) \tag{1}$$

In (1), $u_i(X_k, t)$ is the *displacement vector* and t is the time. Moreover (1) is called the *Lagrangian formulation* which means that x_i, also denoted the *spatial coordinates*, are expressed in terms of the *material coordinates*, X_i. Another formulation is the *Eulerian formulation* where the material coordinates are expressed in terms of the spatial coordinates but since the Lagrangian formulation is the most common formulation in commercial finite element software, the Eulerian formulation will be discussed no further. In the continuation a fixed configuration is considered, i.e. t is constant.

Consider two points A and B in the reference configuration and the same points in the deformed configuration, now denoted A' and B', see fig. 1.

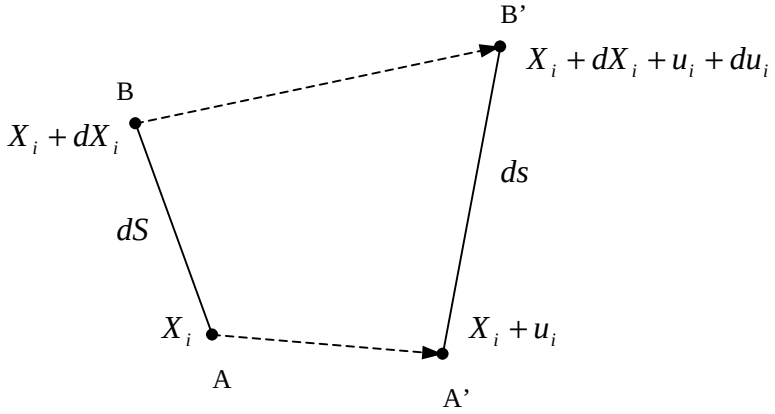

Fig. 1. Two points in the reference and deformed configuration.

The distance between A-B and A'-B', denoted dS and ds respectively, are:

$$\begin{aligned} dS^2 &= dX_i^2 \\ ds^2 &= \left(dX_i + du_i\right)^2 \end{aligned} \tag{2}$$

where $du_i = u_{i,j} dx_j$ and $u_{i,j}$ is defined as:

$$u_{i,j} = \frac{\partial u_i}{\partial X_j} \tag{3}$$

which is denoted the *displacement gradient*. The measure of deformation is considered to be the change in distance between dS^2 and ds^2 i.e.:

$$\begin{aligned} ds^2 - dS^2 &= \left(dX_i + du_i\right)^2 - dX_i^2 \\ &= \left(u_{i,j} + u_{i,j} + u_{k,j} u_{k,j}\right) dX_j dX_i \\ &= 2 dX_i E_{ij} dX_j \end{aligned} \tag{4}$$

which is the exact expression of the change in distance between A-B and A'-B'. The term E_{ij} in (4) is defined as:

$$E_{ij} = \frac{1}{2}\left(u_{i,j} + u_{j,i} + u_{k,j} u_{k,i}\right) \tag{5}$$

and denoted *Green-Lagrange Strain Tensor*. In linear analysis where small displacements are assumed the displacement gradients are small and the quadratic term in (5) is therefore ignored and the Green-Lagrange strain tensor is reduced to the small strain tensor, which will not be discussed in the current study.

Introducing the *deformation gradient* according to:

$$F_{ij} = \frac{\partial x_i}{\partial X_j} \tag{6}$$

and it is easily shown that by using (1) and (6), the Green-Lagrange strain tensor may also be expressed as:

$$E_{kj} = \frac{1}{2}\left(F_{ij} F_{ik} - \delta_{kj}\right) \tag{7}$$

However, the Green-Lagrange strain tensor is not the only way to measure deformation, see for instance [1].
Moreover, if taking the time derivative of the Green-Lagrange strain tensor to obtain the rate of Green-Lagrange strain tensor according to:

$$\dot{E}_{ij} = \frac{1}{2}\left(F_{ki} \dot{F}_{kj} + \dot{F}_{ki} F_{kj} \right) \tag{8}$$

Differentiation of (6) with respect to time and expand it by the chain rule will result in:

$$\dot{F}_{ij} = L_{ik} F_{kj} \tag{9}$$

where:

$$L_{ik} = \frac{\partial v_i}{\partial x_k} \tag{10}$$

and denoted as the *spatial velocity gradient.* The spatial velocity gradient can be divided into a symmetric and an unsymmetric tensor according to:

$$\begin{aligned} D_{ij} &= \frac{1}{2}\left(\frac{\partial v_i}{\partial x_j} + \frac{\partial v_j}{\partial x_i} \right) \\ W_{ij} &= \frac{1}{2}\left(\frac{\partial v_i}{\partial x_j} - \frac{\partial v_j}{\partial x_i} \right) \end{aligned} \tag{11}$$

where D_{ij} is the *Rate of Deformation Tensor* and W_{ij} is the *Spin Tensor*. It can be shown, see [2], that it is only the rate of deformation tensor that determines the deformation rate of the body. Hence, the spin tensor is related to the rigid body rotation of the body. A relationship between the rate of deformation tensor and the rate of Green-Lagrange strain tensor can be established by using (9) in (8) and the realationship becomes:

$$\dot{E}_{ij} = F_{ik} D_{kl} F_{lj} \tag{12}$$

3.3.1 Equation of motion-Balance equation and stress tensors

Mechanical loads that may act on a body can be in the form of a traction vector, t_i i.e. force per unit area, and a body force per unit mass, b_i, for instance gravity. In the current section, three different forms of the balance law with respect to three different stress tensors will be discussed namely *Cauchy*, *first Piola-Kirchhoff* and the *second Piola-Kirchhoff* stress tensor. Many other possible stress tensors exist but the current study only deals with the three mentioned.

Consider an arbitrary body in the current (or deformed) configuration with the volume *v* and surface area *a*. *Newton's second law*, i.e. the balance equation states that:

$$\int_a t_i da + \int_v \rho b_i dv = \int_v \rho \ddot{u}_i dv \tag{13}$$

where ρ is the mass density in the deformed configuration and $\ddot{u}_i$ is the acceleration vector. Moreover, b_i is the body force vector in the deformed configuration. By the use of *Cauchy's formula*, see for instance [3] the traction vector can be expressed as:

$$t_i = \sigma_{ij} n_j \tag{14}$$

In (14), n_j is the normal vector, in the deformed configuration, to the area *a* and σ_{ij} is the *Cauchy's Stress Tensor* which is the physical stress i.e. force per unit area. Inserting (14) in (13) results in:

$$\int_a \sigma_{ij} n_j da + \int_v \rho b_i dv = \int_v \rho \ddot{u}_i dv \tag{15}$$

Using the *divergence theorem of Gauss* on the first term in (15) which for an arbitrary tensor c_{ij} states:

$$\int_a c_{ij} n_j da = \int_v c_{ij,j} dv \tag{16}$$

and (15) results in:

$$\int_v \frac{\partial \sigma_{ij}}{\partial x_j} dv + \int_v \rho b_i dv = \int_v \rho \ddot{u}_i dv \tag{17}$$

Since (17) must be valid for an arbitrary body the following must hold:

$$\frac{\partial \sigma_{ij}}{\partial x_j} + \rho b_i = \rho \ddot{u}_i \tag{18}$$

which is the balance equation with Cauchy's stress tensor. Note that it is defined in the current configuration.

To obtain the balance equation in the reference configuration, consider that the current force can, by the use of (14), be written as:

$$t_i da = \sigma_{ij} n_j da \tag{19}$$

Making use of *Nanson's formula* according to:

$$n_i da = J F_{ji}^{-1} n_j^o dA \tag{20}$$

where n_j^o is the normal vector in the reference configuration and *J* is the determinant of the deformation gradient and denoted the *Jacobian*. With (20), (19) now becomes:

$$t_i da = \sigma_{ik} J F_{jk}^{-1} n_j^o dA \tag{21}$$

The first Piola-Kirchhoff stress tensor can now be defined according to:

$$P_{ij} = J \sigma_{ik} F_{jk}^{-1} \tag{22}$$

With (14) and (22), (19) becomes:

$$\sigma_{ij} n_j da = P_{ij} n_j^o dA \tag{23}$$

As can be seen, the left-hand side of (23) is the force in the current configuration, while the right-hand side is the force in the reference configuration. By also considering that the mass of the continuum must be constant i.e. conservation of mass:

$$\rho^o dV = \rho dv \tag{24}$$

Proceeding by inserting (23) into (15) and use (24). Then, by using Nanson's formula (20) and since the relationship must hold for arbitrary volumes, the balance with the first Piola-Kirchhoff stress tensor becomes:

$$\frac{\partial P_{ij}}{\partial X_j} + \rho^o b_i^o = \rho^o \ddot{u}_i \tag{25}$$

where b_i^o is the body force per unit mass in the reference configuration. One major disadvantage is that the first Piola-Kirchhoff stress tensor is usually not symmetric which makes it expensive to use. However, if multiplying (22) with F_{li}^{-1} and a symmetric tensor is obtained i.e. *the second Piola-Kirchhoff stress tensor* according to:

$$S_{lj} = F_{li}^{-1} P_{ij} = J F_{li}^{-1} \sigma_{ik} F_{jk}^{-1} \tag{26}$$

where in (26), the relationship between the second Piola-Kirchhoff stress tensor and Cauchy's stress tensor also was established. By using (26) and (25) and rewriting the deformation gradient according to (6) the following is obtained:

$$\frac{\partial}{\partial X_j}\left(S_{lj} F_{il}\right) + \rho^o b_i^o = \rho^o \ddot{u}_i \tag{27}$$

which is the balance equation with the second Piola-Kirchhoff stress tensor. Note that it is defined in the reference configuration.

3.3.2 The principle of virtual power

In the previous section three different forms of the balance equations were derived with respect to chosen stress tensor. The results are denoted as the *strong form* and in the current chapter the *weak form* will be derived by using the principle of virtual power. As starting point, (18) is multiplied with an arbitrary weight function, w_i i.e. a *virtual velocity* (due to virtual power), i.e.:

$$w_i \frac{\partial \sigma_{ij}}{\partial x_j} + w_i \rho b_i = w_i \rho \ddot{u}_i \tag{28}$$

Now, by elaborating an expression like:

$$\frac{\partial}{\partial x_j}\left(w_i \sigma_{ij}\right) = \frac{\partial w_i}{\partial x_j} \sigma_{ij} + w_i \frac{\partial \sigma_{ij}}{\partial x_j}$$

and perform integration by parts on (28) over the volume of the body according to:

$$\int_v \frac{\partial}{\partial x_j}\left(w_i \sigma_{ij}\right) dv - \int_v \frac{\partial w_i}{\partial x_j}\sigma_{ij}\, dv + \int_v w_i \rho b_i\, dv = \int_v w_i \rho \ddot{u}_i\, dv \tag{29}$$

Using (16) and (14) on the first term in (29) according to:

$$\int_v (w_i \sigma_{ij})_{,j}\, dv = \int_a w_i \sigma_{ij} n_j\, da = \int_a w_i t_i\, da \tag{30}$$

Studying the second term in (29). Since σ_{ij} is a symmetric tensor and the trace of a product of a symmetric tensor times an antisymmetric tensor vanish, the symmetric part of $\frac{\partial w_i}{\partial x_j}$ is introduced according to:

$$D_{ij}^{w} = \frac{1}{2}\left(\frac{\partial w_i}{\partial x_j} + \frac{\partial w_j}{\partial x_i}\right) \tag{31}$$

The quantity D_{ij}^{w} shall be interpreted as the *rate of deformation tensor with respect to the virtual velocity*. Now, with (30) and (31), (29 b) results in:

$$\int_a w_i t_i\, da - \int_v D_{ij}^{w}\sigma_{ij}\, dv + \int_v w_i \rho b_i\, dv = \int_v w_i \rho b_i \ddot{u}_i\, dv \tag{32}$$

With the relationship in (12) but now for the rate of deformation tensor with respect to the virtual velocity, i.e.:

$$\dot{E}_{st}^{w} = F_{is} D_{ij}^{w} F_{jt} \tag{33}$$

with (26) and (33), equation (32) result in:

$$\int_v w_i \rho \ddot{u}_i\, dv + \int_V \dot{E}_{ij}^{w} S_{ij}\, dV - \int_a w_i t_i\, da - \int_v w_i \rho b_i\, dv = 0 \tag{34}$$

which is the weak form of (27). Note that by expanding (31) by the chain-rule and together with (33) and the second term in (34) is now defined in the reference configuration. To transform the remaining terms in (34) to the reference configuration, consider that the traction vector in the deformed configuration is defined as the current force divided by the current area. Thus the traction vector in the reference configuration, denoted t_i^o should be defined as the reference force divided by the reference area, *dA* i.e.:

$$t_i^o\, dA = t_i\, da \tag{35}$$

By using (24) and (35), the equation (34) can be expressed in the reference configuration according to:

$$\int_V w_i \rho^o \ddot{u}_i\, dV + \int_V \dot{E}_{ij}^{w} S_{ij}\, dV + \int_A w_i t_i^o\, dA - \int_V w_i \rho^o b_i\, dV = 0 \tag{36}$$

which is the principle of virtual power with the use of Green-Lagrange strain tensor and the second Piola-Kirchhoff stress tensor and the corresponding weak form of (27). In some literature the corresponding derivation as in the current study is performed by using variations of the Green-Lagrange strain tensor, see for instance [4].

3.2 The Finite Element Formulation - Large Deformations

In this section a finite element formulation with respect to large deformations with starting point according to (36) will be carried out. For simplicity, only plane conditions are considered and (36) is presented in matrix format as the starting point of the derivation:

$$\int_V \rho^o \mathbf{w}^{\mathbf{T}} \ddot{\mathbf{u}} dV + \int_V \dot{\mathbf{E}}^{w\mathbf{T}} \mathbf{S} dV - \int_A \mathbf{w}^{\mathbf{T}} \mathbf{t}^o dA - \int_V \rho^o \mathbf{w}^{\mathbf{T}} \mathbf{b} dV = 0 \tag{37}$$

with the following notations:

$$\dot{\mathbf{E}}^w = \begin{bmatrix} \dot{E}_{11}^w \\ \dot{E}_{22}^w \\ 2\dot{E}_{12}^w \end{bmatrix} \qquad \mathbf{S} = \begin{bmatrix} S_{11} \\ S_{22} \\ S_{12} \end{bmatrix} \qquad \ddot{\mathbf{u}} = \begin{bmatrix} \ddot{u}_1 \\ \ddot{u}_2 \end{bmatrix} \qquad \mathbf{w} = \begin{bmatrix} w_1 \\ w_2 \end{bmatrix} \qquad \mathbf{t}^o = \begin{bmatrix} t_1^o \\ t_2^o \end{bmatrix} \qquad \mathbf{b}^o = \begin{bmatrix} b_1^o \\ b_2^o \end{bmatrix} \tag{38}$$

The displacement vector, **u**, is in the finite element method approximated as:

$$\mathbf{u} = \mathbf{N}\mathbf{a} \tag{39}$$

where **N** is the *global shape function* depending on which element formulation used and **a** is a vector containing all nodal displacements.
According to (1), the displacement vector **u** is a function of both position and time and the shape function is only a function of position, see for instance [5], i.e.:

$$\mathbf{u} = \mathbf{u}(X_i, t) \qquad \mathbf{N} = \mathbf{N}(X_i) \qquad \mathbf{a} = \mathbf{a}(t) \tag{40}$$

Thus the following is valid:

$$\ddot{\mathbf{u}} = \mathbf{N}\ddot{\mathbf{a}} \tag{41}$$

From (8) with (1) it follows that (33) can be expressed according to:

$$\dot{E}_{st}^w = \frac{1}{2}\left(\frac{\partial w_s}{\partial X_t} + \frac{\partial w_t}{\partial X_s}\right) + \frac{1}{2}\left(\frac{\partial u_i}{\partial X_s}\frac{\partial w_i}{\partial X_t} + \frac{\partial w_j}{\partial X_s}\frac{\partial u_j}{\partial X_t}\right) \tag{42}$$

Expanding (42) for a plane case shows that (42) can be simplified by introducing one linear and one nonlinear operator according to:

$$\nabla_{\mathbf{o}}\mathbf{w} = \begin{bmatrix} \dfrac{\partial}{\partial X_1} & 0 \\ 0 & \dfrac{\partial}{\partial X_2} \\ \dfrac{\partial}{\partial X_2} & \dfrac{\partial}{\partial X_1} \end{bmatrix} \begin{bmatrix} w_1 \\ w_2 \end{bmatrix} \tag{43}$$

$$\nabla_{\mathbf{u}}\mathbf{w} = \begin{bmatrix} \dfrac{\partial u_1}{\partial X_1}\dfrac{\partial}{\partial X_1} & \dfrac{\partial u_2}{\partial X_1}\dfrac{\partial}{\partial X_1} \\ \dfrac{\partial u_1}{\partial X_2}\dfrac{\partial}{\partial X_2} & \dfrac{\partial u_2}{\partial X_2}\dfrac{\partial}{\partial X_2} \\ \dfrac{\partial u_1}{\partial X_1}\dfrac{\partial}{\partial X_2} + \dfrac{\partial u_1}{\partial X_2}\dfrac{\partial}{\partial X_1} & \dfrac{\partial u_2}{\partial X_1}\dfrac{\partial}{\partial X_2} + \dfrac{\partial u_2}{\partial X_2}\dfrac{\partial}{\partial X_1} \end{bmatrix} \tag{44}$$

I.e. with the strain vector in (38) and the introduced operators, (42) becomes:

$$\dot{\mathbf{E}}^{w} = \nabla_{\mathbf{o}}\mathbf{w} + \nabla_{\mathbf{u}}\mathbf{w} \tag{45}$$

To be able to proceed, the weight function, **w** must be chosen. Different ways to approximate **w** exist, for instance *the point collocation method* or *the subdomain collocation method*, see for instance [4] or [6]. However in the current study the weight vector is chosen according to *Bubnov-Galerkin* or simply *the Galerkin method* where the weight vector is approximated in the same manner as the displacement vector in (39), i.e.:

$$\mathbf{w} = \mathbf{N}\mathbf{c} \tag{46}$$

where **c** like **w** is an arbitrary vector with the exception that **w** is a function of position and time and **c** is function of time only. Using (46) with (43) and (44) in (42) yields (in matrix format):

$$\dot{\mathbf{E}}^{w} = \left(\nabla_{\mathbf{o}}\mathbf{N} + \nabla_{\mathbf{u}}\mathbf{N}\right)\mathbf{c} = \left(\mathbf{B}_{\mathbf{o}} + \mathbf{B}_{\mathbf{u}}\right)\mathbf{c} \tag{47}$$

By inserting (46) in (42) it is realized that $\mathbf{B_o}$ is a function of the material coordinates and $\mathbf{B_u}$ (in general) depend on the displacements i.e. $\mathbf{B_o}=\mathbf{B_o}(X_i)$ and $\mathbf{B_u}=\mathbf{B_u}(u_i, X_i)$. To simplify the notation, the following is defined:

$$\mathbf{B} = \mathbf{B}_{\mathbf{o}} + \mathbf{B}_{\mathbf{u}} \tag{48}$$

Proceeding by using (41), (46) and (48) in (37) and move **c** outside the brackets result in:

$$\mathbf{c}^{T}\left[\int_V \rho^{o}\mathbf{N}^{\mathbf{T}}\mathbf{N}\ddot{\mathbf{a}}dV + \int_V \mathbf{B}^{\mathbf{T}}\mathbf{S}dV - \int_A \mathbf{N}^{\mathbf{T}}\mathbf{t}^{\mathbf{o}}dA - \int_V \rho^{o}\mathbf{N}^{\mathbf{T}}\mathbf{b}^{\mathbf{o}}dV\right] = 0 \tag{49}$$

Since (49) must hold for arbitrary **c**-matrices, (49) must become:

$$\int_V \rho^{o}\mathbf{N}^{\mathbf{T}}\mathbf{N}dV\ddot{\mathbf{a}} + \int_V \mathbf{B}^{\mathbf{T}}\mathbf{S}dV - \int_A \mathbf{N}^{\mathbf{T}}\mathbf{t}^{\mathbf{o}}dA - \int_V \rho^{o}\mathbf{N}^{\mathbf{T}}\mathbf{b}^{\mathbf{o}}dV = \mathbf{0} \tag{50}$$

The *mass matrix* **M** can be defined from the first term (50) according to:

$$\mathbf{M} = \int_V \rho^o \mathbf{N}^\mathbf{T} \mathbf{N} dV \tag{51}$$

the *external forces* are given by the traction vector $\mathbf{t^o}$ and the body force vector $\mathbf{b^o}$ according to:

$$\mathbf{f}_{ext} = \int_A \mathbf{N}^\mathbf{T} \mathbf{t}^\mathbf{o} dA + \int_V \rho^o \mathbf{N}^\mathbf{T} \mathbf{b}^\mathbf{o} dV \tag{52}$$

and finally the *internal forces* in the continuum due to the applied load:

$$\mathbf{f}_{\text{int}} = \int_V \mathbf{B}^\mathbf{T} \mathbf{S} dV \tag{53}$$

With the above introduced expressions, (50) is reduced to:

$$\mathbf{G} = \mathbf{M}\ddot{\mathbf{a}} + \mathbf{f}_{\text{int}} - \mathbf{f}_{ext} = \mathbf{0} \tag{54}$$

i.e. for equilibrium to hold: the external forces must be equal the internal forces plus the inertial forces (Newton's second law). The quantity **G** is denoted *the Residual Force Vector*. As can be seen in (50) no constitutive model has been introduced. Therefore (54) is valid for any constitutive law chosen.

3.3 Static loading conditions

Static analysis can only be performed using the implicit finite element method, see for instance [3] and [7] where the nonlinear implicit finite element scheme is thoroughly described. The *equilibrium equation* (54) is valid for dynamic conditions. For static or quasi-static analysis, for instance sheet metal forming analysis, where inertial effects can be neglected the mass-matrix is simply put equal to zero. As stated in the pervious section, no constitutive law was introduced to obtain (54). In the current section, it is assumed that the stress can be linearized and that the stress increment is defined as d**S**=**D**d**E**.

For nonlinear geometry, it is known that the Green-Lagrange strain tensor is nonlinear (due to the quadratic term in (5)), (54) also becomes nonlinear. Therefore (54) cannot directly be solved which would have been the case if the small strain tensor had been used. Instead an iterative solution must be used, usually based on the *Newton-Raphson Method*, see for instance [7]. To obtain an iterative format based on the Newton-Raphson method a Taylor expansion of (54) around an equilibrium point is made. Assuming static conditions and the Taylor expansion of (54) around an equilibrium point, **a**, becomes:

$$\mathbf{G}(\mathbf{a} + d\mathbf{a}) = \mathbf{G(a)} + d\mathbf{G(a)} = \mathbf{0} \tag{55}$$

Assuming that the external load, $\mathbf{f}_{ext}$ is not depending on nodal displacements, the second term of (55) is in comparison with (54) recognized as:

$$d\mathbf{G} = d\mathbf{f}_{\text{int}} \tag{56}$$

i.e. (55) becomes:

$$\mathbf{G}(\mathbf{a}) + d\mathbf{f}_{\text{int}}(\mathbf{a}) = \mathbf{0} \tag{57}$$

Recall (53) and (56) becomes:

$$d\mathbf{f}_{\text{int}} = \int_V d\mathbf{B}^{\mathbf{T}}\mathbf{S}dV + \int_V \mathbf{B}^{\mathbf{T}}d\mathbf{S}dV \tag{58}$$

As can be seen in (58) the first term deals with the change of the **B**-matrix i.e. the geometry and the second term deals with the change of the stresses. Examining the terms in (58) and recalling (48) where $\mathbf{B_0}$ in **B** only contain material coordinates i.e. constants, results in $d\mathbf{B_0}=\mathbf{0}$. But since $\mathbf{B_u}$ in (48) depends on the displacements so does **B** and since $\mathbf{f}_{int}$ is highly controlled by the nodal displacements, **B** must be differentiated i.e.:

$$d\mathbf{B} = d\mathbf{B_u} \tag{59}$$

One way to formulate $\mathbf{B_u}$ in matrix-format is according to:

$$\mathbf{B}_u = \nabla_u \mathbf{N} = \begin{bmatrix} \frac{\partial u_1}{\partial X_1} & 0 & \frac{\partial u_2}{\partial X_1} & 0 \\ 0 & \frac{\partial u_1}{\partial X_2} & 0 & \frac{\partial u_2}{\partial X_2} \\ \frac{\partial u_1}{\partial X_2} & \frac{\partial u_1}{\partial X_1} & \frac{\partial u_2}{\partial X_2} & \frac{\partial u_2}{\partial X_1} \end{bmatrix} \begin{bmatrix} \frac{\partial N_1}{\partial X_1} \\ \frac{\partial N_1}{\partial X_2} \\ \frac{\partial N_2}{\partial X_1} \\ \frac{\partial N_2}{\partial X_2} \end{bmatrix} = \mathbf{AH} \tag{60}$$

Having introduced **AH** it can be shown that the first term in (58) can be written as:

$$d\mathbf{B}^{\mathbf{T}}\mathbf{S} = \mathbf{H}^{\mathbf{T}}\mathbf{R}\mathbf{H}d\mathbf{a} \tag{61}$$

where:

$$\mathbf{R} = \begin{bmatrix} \bar{\mathbf{S}} & \mathbf{0} \\ \mathbf{0} & \bar{\mathbf{S}} \end{bmatrix} \qquad \bar{\mathbf{S}} = \begin{bmatrix} S_{11} & S_{12} \\ S_{21} & S_{22} \end{bmatrix} \tag{62}$$

The second term in (58) are established as follows:

$$\mathbf{B}^{\mathbf{T}}d\mathbf{S} = \mathbf{B}^{\mathbf{T}}\mathbf{D}d\mathbf{E} = \mathbf{B}^{\mathbf{T}}\mathbf{D}\mathbf{B}d\mathbf{a} \tag{63}$$

Finally, by inserting (61) and (63) in (58) and then (55) yields:

$$\begin{gathered} \mathbf{G}(\mathbf{a}) + \left(\int_V \mathbf{B}^{\mathbf{T}}\mathbf{D}\mathbf{B}dV + \int_V \mathbf{H}^{\mathbf{T}}\mathbf{R}\mathbf{H}dV \right) d\mathbf{a} = \mathbf{0} \\ \Leftrightarrow \\ \mathbf{G}(\mathbf{a}) + \mathbf{K}d\mathbf{a} = \mathbf{0} \end{gathered} \tag{64}$$

where the stiffness matrix for large deformations under static loading conditions was established i.e.:

$$\mathbf{K} = \int_V \mathbf{B}^{\mathrm{T}}\mathbf{D}\mathbf{B}dV + \int_V \mathbf{H}^{\mathrm{T}}\mathbf{R}\mathbf{H}dV \tag{65}$$

Consider the two terms in (65) and it is evident that the first term is related to the constitutive law whereas the second term is due to that nonlinear strain measures are taken into account, i.e. large deformations.

3.4 Dynamic loading conditions

When it comes to solving dynamic problems, using the finite element method, time integration must be performed. Today there are two major time integration algorithms for solving dynamic problems using the finite element method: the *implicit* and the *explicit* method. The time integration is basically the same for both algorithms but the big difference is how the algebraic equations are solved. As will be shown in the next section, where the explicit finite element method is discussed, the nodal displacements are obtained naturally by the use of the approximations introduced by Newmark, together with some choices of parameters. However, the calculation of the strains and the stresses are exactly the same for both methods.

Considering dynamic loading situations, an integration of time must be performed. Recalling (54) i.e. the equation of motion and in the meantime also introduce damping, **C**, into the system:

$$\mathbf{M}\ddot{\mathbf{a}} + \mathbf{C}\dot{\mathbf{a}} + \mathbf{f}_{\mathrm{int}}(\mathbf{a}) - \mathbf{f}_{ext}(t) = \mathbf{0} \tag{66}$$

In the current study Rayleigh damping is assumed:

$$\mathbf{C} = d_1\mathbf{M} + d_2\mathbf{K} \tag{67}$$

where d_1 and d_2 are constants, usually determined experimentally. To transform the nonlinear differential equations in (66) into algebraic equations, the *Newmark time integration scheme* proposed by Newmark (1959) will be used.

Newmark introduced the following approximations of $\dot{\mathbf{a}}_{n+1}$ and $\ddot{\mathbf{a}}_{n+1}$ according to:

$$\begin{aligned} \mathbf{a}_{n+1} &= \mathbf{a}_n + \Delta t\,\dot{\mathbf{a}}_n + \frac{\Delta t^2}{2}\left[(1-2\beta)\ddot{\mathbf{a}}_n + 2\beta\,\ddot{\mathbf{a}}_{n+1}\right] \\ \dot{\mathbf{a}}_{n+1} &= \dot{\mathbf{a}}_n + \Delta t\left[(1-\gamma)\ddot{\mathbf{a}}_n + \gamma\,\ddot{\mathbf{a}}_{n+1}\right] \end{aligned} \tag{68}$$

where β and γ are certain parameters, see for instance [1].
Suppose that everything is known at state $\mathbf{a}_n$. The next state to be determined is $\mathbf{a}_{n+1}$, i.e. (66) will be:

$$\mathbf{M}\ddot{\mathbf{a}}_{n+1} + \mathbf{C}\dot{\mathbf{a}}_{n+1} + \mathbf{f}_{\mathrm{int}}(\mathbf{a}_{n+1}) - \mathbf{f}_{ext(n+1)} = \mathbf{0} \tag{69}$$

Rewriting (68) to obtain:

$$\begin{aligned}\ddot{\mathbf{a}}_{n+1} &= c_1\mathbf{a}_{n+1} - c_1\mathbf{a}_n - c_2\dot{\mathbf{a}}_n - c_3\ddot{\mathbf{a}}_n \\ \dot{\mathbf{a}}_{n+1} &= c_4\mathbf{a}_{n+1} - c_4\mathbf{a}_n - c_5\dot{\mathbf{a}}_n - c_6\ddot{\mathbf{a}}_n\end{aligned} \tag{70}$$

where the introduced c_i-parameters are:

$$\begin{aligned} c_1 &= \frac{1}{\beta\Delta t^2} \quad c_2 = \frac{1}{\beta\Delta t} \quad c_3 = \frac{1-2\beta}{2\beta} \\ c_4 &= \frac{\gamma}{\beta\Delta t} \quad c_5 = \frac{\gamma-\beta}{\beta} \quad c_6 = \Delta t\frac{\gamma-2\beta}{2\beta}\end{aligned}$$

For simplicity, the damping in (67) are assumed to only depend on the mass-matrix i.e. d_2 in (67) is set to zero which will be an evident choice in the section where the explicit finite element formulation is discussed. Using (70) in (69) will in the step $\mathbf{a}_{n+1}$ become:

$$(c_1 + d_1c_4)\mathbf{M}\mathbf{a}_{n+1} + \mathbf{f}_{\text{int}}(\mathbf{a}_{n+1}) + \mathbf{f}_{ext(n+1)} - \mathbf{M}\ddot{\mathbf{a}}'_n = \mathbf{0} \tag{71}$$

where:

$$\ddot{\mathbf{a}}'_n = c_1\mathbf{a}_n + c_2\dot{\mathbf{a}}_n + c_3\ddot{\mathbf{a}}_n + d_1c_4\mathbf{a}_n + d_1c_5\dot{\mathbf{a}}_n + d_1c_6\ddot{\mathbf{a}}_n$$

Recall (55) i.e.

$$\mathbf{G}(\mathbf{a} + d\mathbf{a}) = \mathbf{G(a)} + d\mathbf{G(a)}$$

and in analogy with static conditions i.e. (56), (71) becomes:

$$d\mathbf{G}_{eff} = (c_1 + d_1c_4)\mathbf{M}d\mathbf{a} + d\mathbf{f}_{\text{int}} = \mathbf{0} \tag{72}$$

where it is noted that the mass-matrix is constant due to that the shape functions are constant and the external forces do not depend on the displacement. Recall (58) and (64), i.e. $d\mathbf{f}_{int}$ equals the stiffness matrix for static conditions, and (64 b) becomes:

$$\mathbf{G}_{eff} + \mathbf{K}_{eff}d\mathbf{a} = \mathbf{0} \tag{73}$$

where the *effective stiffness matrix*, $\mathbf{K}_{eff}$, was introduced according to:

$$\mathbf{K}_{eff} = (c_1 + d_1c_4)\mathbf{M} + \mathbf{K} \tag{74}$$

As can be seen, the stiffness matrix for dynamic analyses is generated by using the stiffness matrix for static loading situations with a few additions due to the dynamics.

3.5 Explicit Finite Element Method

The current section will show that by some choices, (73) is simplified to the explicit finite element method, which is the most common tool for numerical analysis of vehicle crashworthiness. In comparison with the implicit finite element method where the nodal displacements are calculated by using the stiffness matrix, the nodal displacements are directly obtained from the time integration algorithm, for instance the Newmark time integration algorithm discussed in the previous section. Already now, by considering that d_2

in (67) is put to zero, a major difference between the implicit and the explicit finite element method can be established: the explicit method does not use a stiffness matrix. Recalling the approximations proposed by Newmark in (68).

In the explicit finite element method the following is chosen:

$$\beta = 0 \qquad \gamma = \frac{1}{2} \tag{75}$$

With these choices, Newmark's approximations in (68) become:

$$\mathbf{a}_{n+1} = \mathbf{a}_n + \Delta t\, \dot{\mathbf{a}}_n + \frac{\Delta t^2}{2} \ddot{\mathbf{a}}_n \tag{76}$$

and

$$\dot{\mathbf{a}}_{n+1} = \dot{\mathbf{a}}_n + \frac{\Delta t}{2}\left(\ddot{\mathbf{a}}_n + \ddot{\mathbf{a}}_{n+1} \right) \tag{77}$$

The equation of motion at the current time t_n i.e.:

$$\mathbf{M}\ddot{\mathbf{a}}_n + \mathbf{C}\dot{\mathbf{a}}_n + \mathbf{f}_{\text{int}(n)} + \mathbf{f}_{ext(n)} = \mathbf{0} \tag{78}$$

From (76) the current acceleration, $\ddot{\mathbf{a}}_n$ can be determined:

$$\ddot{\mathbf{a}}_n = \frac{2}{\Delta t^2}\left(\mathbf{a}_{n+1} - \mathbf{a}_n\right) - \frac{2}{\Delta t}\dot{\mathbf{a}}_n \tag{79}$$

With (77) and (79) the nodal velocities, $\dot{\mathbf{a}}_n$ and the nodal accelerations, $\ddot{\mathbf{a}}_n$ can be expressed in terms of nodal displacements according to:

$$\dot{\mathbf{a}}_n = \frac{1}{2\Delta t}\left(\mathbf{a}_{n+1} - \mathbf{a}_{n-1}\right) \qquad \ddot{\mathbf{a}}_n = \frac{1}{\Delta t^2}\left(\mathbf{a}_{n+1} - 2\mathbf{a}_n + \mathbf{a}_{n-1}\right) \tag{80}$$

With the choices done in (75) and consider (80), it is realized that the *central difference approximation* of $\ddot{\mathbf{a}}_n$ is obtained. For more information regarding the central difference method, see for instance [4].

Finally, by inserting (80) into the equation of motion, (78) the following equation system is obtained:

$$\left(\mathbf{M} + \mathbf{C}\frac{\Delta t}{2}\right)\mathbf{a}_{n+1} = \mathbf{M}(2\mathbf{a}_n - \mathbf{a}_{n-1}) - \mathbf{C}\frac{\Delta t}{2}\mathbf{a}_{n-1} - \Delta t^2(\mathbf{f}_{\text{int}(n)} - \mathbf{f}_{ext(n)}) \tag{81}$$

Everything in state *n* is known, and then of course everything at state *n-1* is known, and the next state to be determined is the state *n+1*. Since the mass matrix also is known, (81) provides the solution, i.e. the nodal displacements for state *n+1* directly without any need of iterations. By also turning the mass-matrix into a *lumped* mass-matrix i.e. the mass-matrix

only contains diagonal terms, no inversion of the mass-matrix must be done. Also by setting d_2 in (67) to zero, no stiffness matrix is involved. Therefore only component division has to be performed which is a huge advantage when it comes to computational time demand.

One way to lump the mass-matrix is as adopted by LS-DYNA, the software used in the current study, to simply sum all terms in each row and place the sum so that a diagonal mass-matrix is obtained, [8]. The major disadvantage with the explicit method is that the time step Δt must not be too large to avoid instabilities, see for instance [7].

3.6 Hypo-elastoplasticity

Today two major schools exist for constitutive modeling of plasticity namely *Hyper-elastoplasticity* and *Hypo-elastoplasticity*, see for instance [2]. The most common model when it comes to model plastic response in a material, using the finite element method, is hypo-elastoplasticity, which will be presented in the current chapter. However, it does not (at the present date) exist an officially accepted method, regarding modeling of large strain plasticity,
The plasticity model that will be adopted is the *Isotropic von Mises Hardening* since this model is commonly used when it comes to model plastic response in material during crashworthiness analysis.

The displacements of a continuum can be rigid, elastic or plastic. Disregarding the rigid body motions, since only deformations are of interest, and the displacement vector can be split into an elastic and a plastic part according to:

$$u_i = u_i^e + u_i^p \tag{82}$$

where the superscript "*e*" denotes *elastic* and "*p*" is *plastic* i.e. u_i^e is elastic displacements and u_i^p is the plastic displacements. In small strain plasticity the small strain tensor is divided into an elastic- and a plastic part i.e.:

$$\varepsilon_{ij} = \varepsilon_{ij}^e + \varepsilon_{ij}^p \tag{83}$$

For problems involving nonlinear geometry this separation cannot be done due to the nonlinear contribution. Instead the hypo-formulation states that the velocity vector can be separated into an elastic and a plastic part:

$$v_i = v_i^e + v_i^p \tag{84}$$

and with this separation, the rate of deformation can be formulated as:

$$D_{ij} = D_{ij}^e + D_{ij}^p \tag{85}$$

For small strain plasticity, the stresses are given by the strains via the constitutive law:

$$\dot{\sigma}_{ij} = L_{ijkl}\left(\dot{\varepsilon}_{kl} - \dot{\varepsilon}_{kl}^{\,p} \right)$$

To generalize to large deformation, the stress-strain relationship are formulated as:

$$\overset{o}{\sigma}_{ij} = L_{ijkl}\left(D_{kl} - D_{kl}^{p}\right)$$
$$L_{ijkl} = 2G\left[\frac{1}{2}\left(\delta_{ik}\delta_{jl} + \delta_{il}\delta_{jk}\right) + \frac{\upsilon}{1-2\upsilon}\delta_{ij}\delta_{kl}\right] \tag{86}$$

where in (86), $\overset{o}{\sigma}_{ij}$ is the *Jaumann stress rate* defined as:

$$\overset{o}{\sigma}_{ij} = \dot{\sigma}_{ij} - W_{im}\sigma_{mj} + \sigma_{im}W_{jm} \tag{87}$$

where $\dot{\sigma}_{ij}$ is the rate of Cauchy's stress tensor. Moreover L_{ijkl} in (86) is an isotropic tensor, G is the shear modulus and υ is Poisson's ratio.

The von Mises isotropic hardening yield criterion, see for instance [3], states that:

$$f = \sqrt{3J_2} - \sigma_y(K) = 0 \tag{88}$$

where:

$$J_2 = \frac{1}{2}s_{ij}s_{ij}$$
$$s_{ij} = \sigma_{ij} - \frac{1}{3}\sigma_{kk}\delta_{ij} \tag{89}$$

where s_{ij} is denoted the *deviatoric stress tensor* of the Cauchy stress, σ_y is the yield limit and K is some hardening parameter that form the *hardening rule* i.e. the rule for how the yield surface changes with the plastic loading. Isotropic hardening is characterized by the fact that the position and shape of the yield surface remains fixed whereas the size of the yield surface changes with the plastic deformation, see for instance [3] and figure 2.

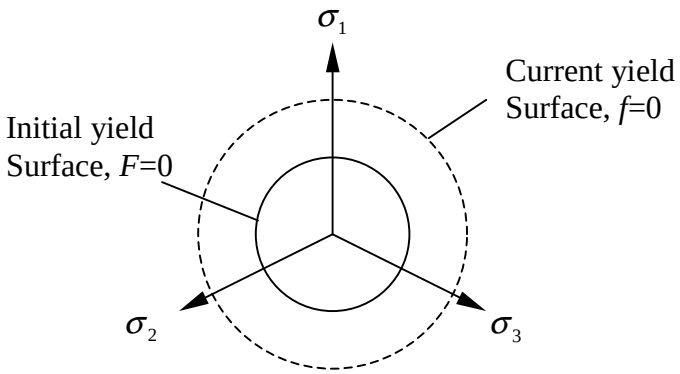

Fig. 2. Isotropic hardening of the von Mises criterion.

If a point is within the yield surface the point behaves elastic and if the point is on the yield surface, the material point behaves plastic. Therefore, during plastic loading the following must be fulfilled:

$$f(\sigma_{ij}, K) = \sigma_{eff} - \sigma_y = 0 \tag{90}$$

where σ_{eff} is the *effective stress* defined according to:

$$\sigma_{eff} = \sqrt{\frac{3}{2} s_{ij} s_{ij}} = \sqrt{3J_2} \tag{91}$$

Formulating the so-called *consistency relation* according to:

$$\dot{f} = 0 \tag{92}$$

and by the use of the chain rule and (92), (90) becomes:

$$\dot{f} = \frac{\partial f}{\partial \sigma_{ij}} \dot{\sigma}_{ij} + \frac{\partial f}{\partial K} \dot{K} = 0 \tag{93}$$

The interpretation of the consistency relation is that during plastic loading, when the stress state varies, so does also the hardening parameter, *K*, in such a manner that the stress state always remains on the yield surface. Consider the first term in (93). An important relationship can be established by multiplying the definition of the Jaumann stress tensor, (87) by s_{ij} and using the definition of the deviatoric stress tensor in (89). This will result in the relation:

$$s_{ij} \overset{o}{\sigma}_{ij} = s_{ij} \dot{\sigma}_{ij} \tag{94}$$

Hence, the following must hold:

$$\frac{\partial f}{\partial \sigma_{ij}} \overset{o}{\sigma}_{ij} = \frac{\partial f}{\partial \sigma_{ij}} \dot{\sigma}_{ij} \tag{95}$$

The *associated flow rule*, see for instance [2], states:

$$D_{ij}^p = \dot{\lambda} \frac{\partial f}{\partial \sigma_{ij}} = \dot{\lambda} \frac{3 s_{ij}}{2 \sigma_y} \tag{96}$$

where $\dot{\lambda}$ is denoted the *plastic multiplier*. Defining the *effective plastic strain rate*:

$$D_{eff}^p = \left(\frac{2}{3} D_{ij}^p D_{ij}^p \right)^{\frac{1}{2}} \tag{97}$$

Using (96) into (97) with the use of (89) will result in:

$$D_{eff}^p = \dot{\lambda} \tag{98}$$

Proceeding with the definition of the *effective plastic strain*:

$$\varepsilon_{eff}^{p} = \int_{0}^{t} D_{eff}^{p}\, dt \qquad \text{or} \qquad \dot{\varepsilon}_{eff}^{p} = D_{eff}^{p} = \dot{\lambda} \tag{99}$$

Moreover, *strain hardening* is chosen i.e. the hardening is controlled by the effective plastic strains which for the hardening parameter in (93) means:

$$\dot{K} = \dot{\varepsilon}_{eff}^{p} \tag{100}$$

Now, with the choice (100) and (99 b) the second term in (93) can be reformulated according to:

$$\frac{\partial \sigma_y}{\partial K}\dot{K} = \frac{\partial \sigma_y}{\partial \varepsilon_{eff}^{p}}\dot{\lambda} \tag{101}$$

Finally, the consistency relation becomes:

$$\dot{f} = \frac{3s_{ij}}{2\sigma_y}\dot{\sigma}_{ij} - H\,\dot{\lambda}$$

where: (102)

$$H = \frac{\partial \sigma_y}{\partial \varepsilon_{eff}^{p}}$$

and H is the plastic modulus that has to be determined from experimental data, see [2]. Referring to the relationship in (94), the consistency relation in (102) can be written as:

$$\frac{3s_{ij}}{2\sigma_y}\overset{o}{\sigma}_{ij} - H\,\dot{\lambda} = 0 \tag{103}$$

To determine the plastic multiplier, $\dot{\lambda}$, (103) is combined with (86) and (96) which, after a few calculations, result in:

$$\dot{\lambda} = \frac{3G}{A\sigma_y} s_{kl} D_{kl}$$

where: (104)

$$A = 3G + H$$

and finally by using (96) and (104) in (86) and after some calculation the following is obtained:

$$\overset{o}{\sigma}_{ij} = L_{ijkl}^{ep} D_{kl}$$

$$L_{ijkl}^{ep} = L_{ijkl} - \frac{9G^2}{A\sigma_y^2} s_{ij} s_{kl} \tag{105}$$

In (105), L_{ijkl} is an isotropic tensor defined in (86) and L^{ep}_{ijkl} is the *elasto-plastic stiffness tensor*. From a purely numerical point of view, the difference between elasto-plastic stiffness tensor and the constitutive law is that the stresses are obtained via the strains and the constitutive law whereas the functionality of the elasto-plastic stiffness tensor only is for generating the stiffness matrix, see the first term in (65) where **D** is the constitutive tensor. However, since (105) involves the Cauchy stress tensor (via the deviatoric stress), it is defined in the current configuration. Since the Lagrangian formulation, see (1), is the most frequently used formulation, the rate of the second Piola-Kirchhoff stress tensor, $\dot{S}_{ij}$, and the rate of the Green-Lagrange strain tensor, $\dot{E}_{ij}$, must be fit into (106). Without going into the signification of *objective tensors*, instead it is refererred to [2] where it is shown that the rate of the second Piola-Kirchhoff stress tensor is described in an similar manner as in (26) i.e.:

$$\dot{S}_{ij} = JF^{-1}_{ik}\overset{\Delta}{\sigma}_{kl}F^{-1}_{jl} \tag{105}$$

where $\overset{\Delta}{\sigma}_{kl}$ is the *Truesdell rate of the Cauchy stress, see for instance* [2], defined according to:

$$\overset{\Delta}{\sigma}_{kl} = \dot{\sigma}_{kl} - L_{km}\sigma_{ml} - \sigma_{km}L_{lm} + \sigma_{kl}D_{ss} \tag{106}$$

With (105) and (106) and referring to [2], the final expression of the von Mises isotropic hardening in the Lagrangian formulation is presented as:

$$\begin{aligned}
&\dot{S}_{ij} = D^{ep}_{ijst}\dot{E}_{st}\\
&D^{ep}_{ijst} = F^{-1}_{ik}F^{-1}_{jl}\tilde{D}_{klmn}F^{-1}_{sm}F^{-1}_{tn}\\
&\tilde{D}_{klmn} = L^{ep}_{klmn} - \frac{1}{2}\left(\delta_{nk}\sigma_{ml} + \delta_{mk}\sigma_{nl} + \sigma_{km}\delta_{nl} + \sigma_{kn}\delta_{ml}\right)\\
&L^{ep}_{ijkl} = L_{ijkl} - \frac{9G^2}{A\sigma_y^2}S_{ij}S_{kl}\\
&L_{ijkl} = 2G\left[\frac{1}{2}\left(\delta_{ik}\delta_{jl} + \delta_{il}\delta_{jk}\right) + \frac{\upsilon}{1-2\upsilon}\delta_{ij}\delta_{kl}\right]
\end{aligned} \tag{107}$$

where D^{ep}_{ijst} is symmetric i.e. $D^{ep}_{ijst} = D^{ep}_{stij}$.

4. Analysis

The current chapter describes the hardware and software, the finite element model used and the crash case that was studied. Moreover a general description of how the optimization software LS-OPT works is presented and how it has been applied in the current study.

4.1 Hardware and Software

The computer used for the analysis was Bombardier Transportation's Compaq HPC 200 with Alpha EV6@667MHz. Each simulation was a single CPU job and the number of simultaneous jobs varied between four and seven depending on the number of available processors and LS-DYNA licenses. The finite element model was generated in Patran, a pre- and post-processor developed by the MacNeal-Schwendler Corporation with CAD-geometry from Pro/Engineer. The solvers used were LS-DYNA, which is an explicit finite element code for three-dimensional nonlinear transient analysis, and LS-OPT, an optimization program for complex nonlinear problems, for instance crash-analyses. Both LS-DYNA and LS-OPT are developed by Livermore Software Technology Corporation. To evaluate the results, LS-Post together with the graphical interface of LS-OPT, LSOptui was used.

4.2 The Finite Element Model

The FE-model used was the front-structure of Crusaris Regina. The model was taken from the full crash model of the Crusaris Regina and was originally generated in Patran using CAD-models generated in Pro/Engineer. The model consists of a total number of 43556 Belytschko-Tsay shell elements, see [8]. Since the crash-structure is symmetric, only half of the structure was modeled and symmetry boundary conditions were applied. The FE-model is shown in figure 3.

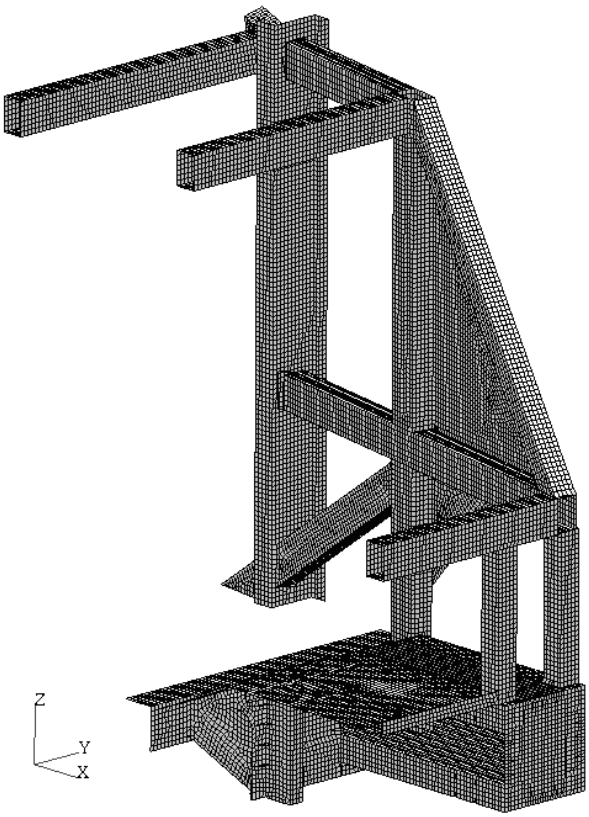

Fig. 3. The FE-model of the crash-structure, Regina Crusaris.

The edge lengths of the elements are between 15-25 mm depending on location with 5 integration points through the thickness of the element.

The material model for all deformable elements was material number 24, Piecewise Linear Isotropic Plasticity, see [8].
The contact definition used was CONTACT_AUTOMATIC_SINGLE_SURFACE, see [12]. The friction between the parts in the model was set to 0.7 and 0.4 for static and dynamic coefficient of friction respectively. These values of the coefficients of friction are commonly used within Bombardier Transportation, Kalmar, Sweden. The front structure is made mainly of mild steel. Regarding material data, the true stress versus true strain curves are presented in the technical report of the crashworthiness analysis of the Crusaris Regina, see [13].

4.3 Crash Load Case

The load case studied is case number three according to the STI-requirements [14] but modified to keep the model and load case as simple as possible. The STI3-requirement as it is originally designed states that the train shall withstand an impact at a speed of 110 km/h with a lorry carrying a load and with a total weight of 15 tons. The lorry and the payload is, in Sweden, represented/simulated by two rigid cylinders where the lower cylinder weighs 5 tons

and is representing the lorry and the upper cylinder weighing 10 tons representing the payload, see figure 4. Hence, since only half the crash-structure is modeled, half the masses of the cylinders were defined i.e. in the FE-model, the upper cylinder weighs 5 tons and the lower weighs 2.5 tons. The cylinders have a diameter of 1 m. and the lower cylinder is located 0.5 m above the top of the rail (TOR), see figure 4.

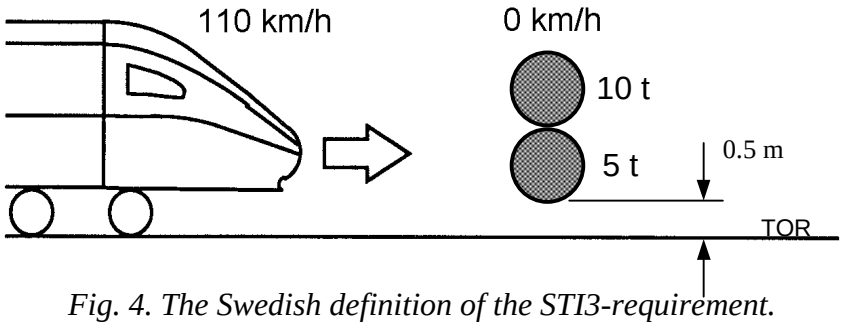

Fig. 4. The Swedish definition of the STI3-requirement.

The structure was designed in such a way that the impact buffers, see figure 5, will absorb the kinetic energy due to the lower cylinder and the beams above the impact buffer will deal with the upper cylinder.

To keep the FE-model and the analysis as simple as possible some simplifications were made. Instead of using a complete train, only the crash-structure is taken into account and the interface of the crash-structure towards the coach is locked in all degrees of freedom. Then, instead of letting the crash-structure run into the cylinders, the cylinders are given an initial velocity towards the crash-structure, see figure 5. As an additional simplification, the intrusions and accelerations were measured on the cylinders instead of the front structure.

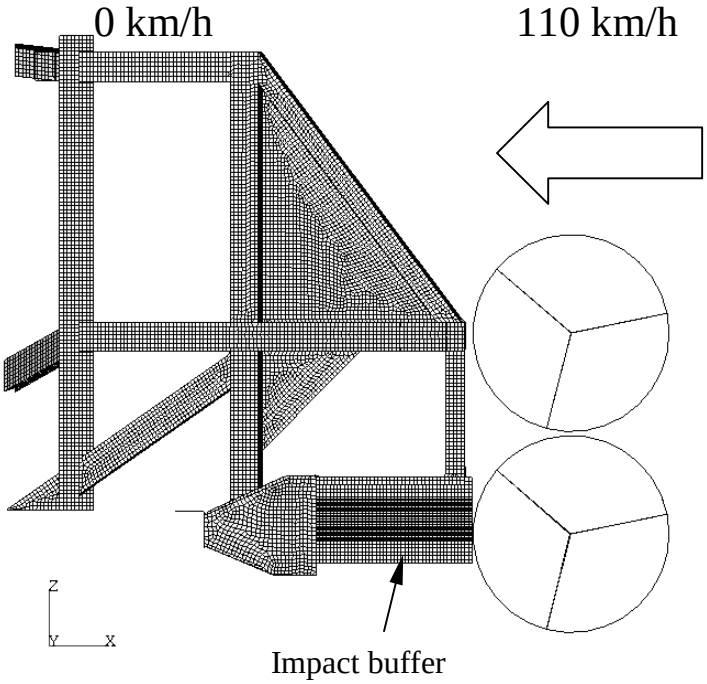

Fig. 5. The impact buffers will absorb the energy from the lower cylinder and the rest of the crash structure will deal with the upper cylinder. The attachments towards the coach are clamped and an initial velocity is applied to the cylinders.

These simplifications will have a major influence on the results. Therefore the results obtained in the current study cannot directly be transferred to the current design of the crash-structure, but the results will give perfectly good hints whether the weight of the crash-structure as a whole can be reduced or not.

4.4 The crash course of event

As stated in the current section, the cylinders impact the crash structure with an initial velocity of 110 km/h. The crash course of event at different time steps is shown in figure 6.

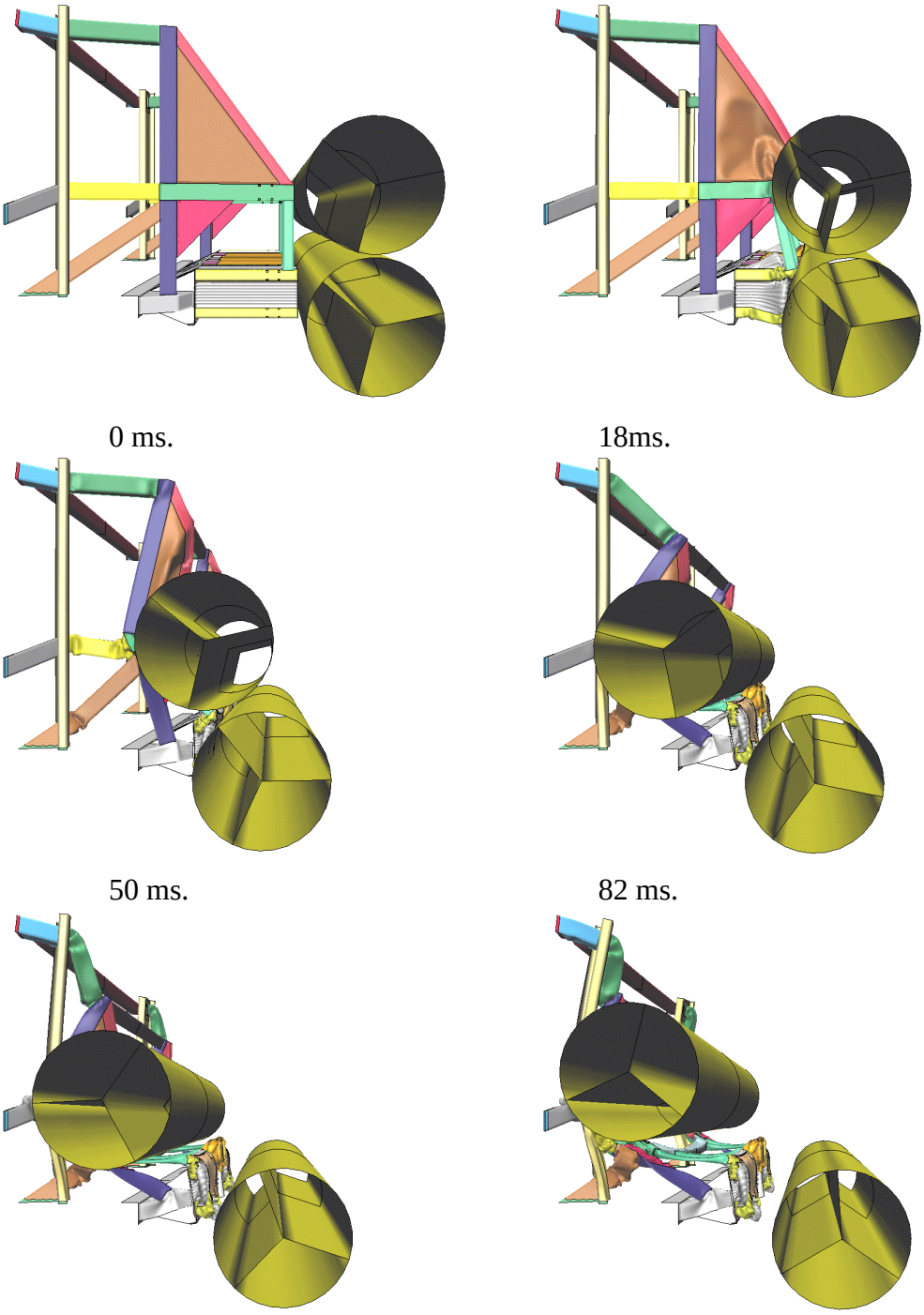

Fig. 6. The deformation of the crash-structure at different time steps.

4.5 Optimization using LS-OPT

4.5.1 General

Structural optimization are divided into three categories:

- *Sizing optimization* - The design variables define a property for instance a thickness of a plate.
- *Shape optimization* - The design variables define the outer dimensions of the geometry.
- *Topology optimization* – In this optimization approach, the geometry is not given an initial design. Only the boundaries where material can be placed are defined.

The optimization problem can mathematically be described as:

$$\min f(x)$$

subjected to:

$$g_j(x) \leq 0; \qquad j = 1,2,.....,m$$

and:

$$h_k(x) = 0; \qquad k = 1,2,.....,l$$

where:

f=Objective function.
g=Inequality constraint function.
h=Equality constraint function.
x=Design variable.
m=*l*=Number of constraint functions.

The optimization method used by LS-OPT is the *Response Surface Methodology* (RSM). RSM is a method for constructing functions that describe the relationship between responses and design variables. These functions are called *Response Surfaces* (RS). To construct the RS, a number of experiments are carried out where the values of the design variables are varied and the responses are recorded. The RS are then fitted to the responses. The RS can be linear or quadratic functions and often the fitting is done by using a least square criteria. To get maximum accuracy in the RS for a given number of experiments, it is important that the experiments are carefully planned. This process is often referred to as *Design Of Experiments* (DOE). Several methods to select the experimental points i.e. perform the DOE, are available in LS-OPT, for instance D-Optimality criteria.

LS-OPT uses RSM to create RS for the objective function and all constraints in the optimization problem. The experiments in this case correspond to LS-DYNA simulations. When LS-OPT has constructed the RS, LS-OPT then solves an approximation of the original optimization problem, where the objective and constraint functions now are described by the RS. Since the RS are approximations of the real problem, the approximations may be overestimated or underestimated. This can result in that the constraints are violated. The result of solving the approximated optimization problem is the result of one *iteration* and hopefully an improved design. LS-OPT has then several methods (e.g. zooming) by which the accuracy of the accuracy of the RS can be improved by performing a new series of experiments and constructing new, more accurate RS and, again, solving an approximation of the original optimization problem. This can be continued until a satisfactory improved design is found.

From a more user point of view, an optimization set up can be described as follows. When defining an optimization analysis using LS-OPT, each design variable is given an initial value i.e. the values of the design variables before any optimization is performed. Then a *range* is defined for each design variable i.e. in what range the optimized solution is to be sought. The domain where an optimum is sought is called the *Design Space*. The design space is reduced, with respect to the range set for all design variables, to obtain the *Region of Interest*, see figure 7. Then a number of *Experimental Points*, depending on the number of design variables used, are distributed over the region of interest. One of the experimental points is based on the initial values of the design variables i.e. the design before any optimization is performed. In the rest of the experimental points, one or more design variables have been changed with respect to the chosen range. This is done in such a way so that as much information as possible is obtained through the experiments. The results from the responses from the experimental points form RS via the RSM. In the current study, a linear approximation was used to create the response surfaces but more advanced approximations are available in LS-OPT, for instance quadratic and elliptical approximations. When the RS are established, LS-OPT sets up an approximate optimization problem, which is solved, and the solution obtained is the result from one iteration. In the next iteration, the region of interest is decreased to increase the accuracy of the RS. For a more thoroughly description of the optimization theory with respect to response surface methodology, see for instance [9] and the references within.

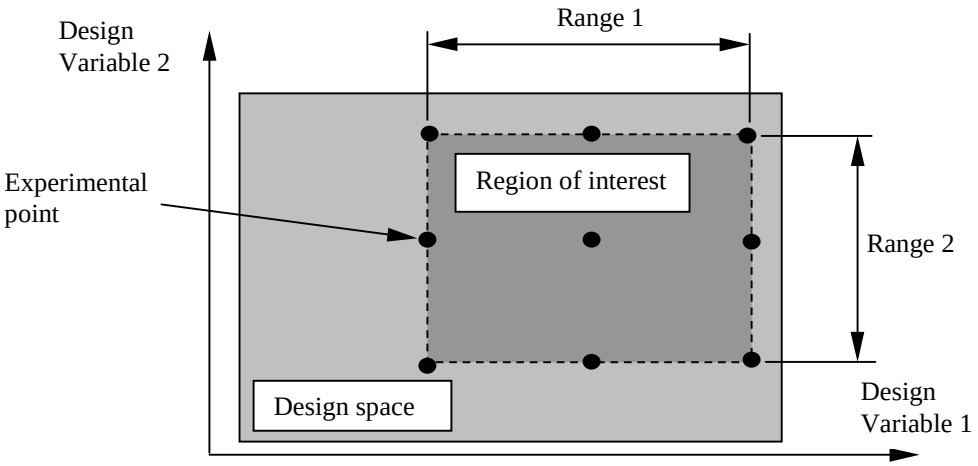

Fig. 7. Design space, region of interest and experimental points.

The chosen range is important since it controls the size of the region of interest, i.e. how much each design variable is allowed to increase or decrease. In each iteration, each design variable is allowed to increase or decrease with half of the defined range. The smaller the range is set the smaller the region of interest and the more accurate the RS become, hence a more accurate result is obtained. But if the range is set too small, the optimization-simulations will be very slow and it would be hard to get a solution in a reasonable amount of time.

The number of experimental points used is of great importance since they also control the accuracy of the RS. The more points used the better the predictive capability of the RS become. LS-OPT has a default value of number of experimental points according to:

*Number of experimental points=(Number of design variables+1)*1.5*

However, according to [10], using the D-optimal design, this is a very rough method of determining the number of experimental points required. The number of experimental points

corresponds to the number of required simulations per iteration plus an extra simulation to check how good the new optimized solution actually became i.e.:

*Total number of simulations=Number of experimental points*Number of iterations+1*

For more information regarding LS-OPT, see [11]

4.5.2 Current study

The objective with the current study is to lower the mass, by performing sizing optimization without worsen the crash performance of the crash structure. The constraint functions were, in the current study, chosen to be the intrusion of respective cylinder and the acceleration levels on each cylinder.

The beams that were to be optimized were chosen on the basis of how important they are to the crash-behavior during impact. Since some beams have other main tasks than absorbing energy during crash, for instance attachment of the cab, these beams are not considered. To keep the CPU-time as low as possible without making the optimization too simple, 12 design variables i.e. 12 beams, were chosen according to figure 8 where the global coordinate system also is shown.

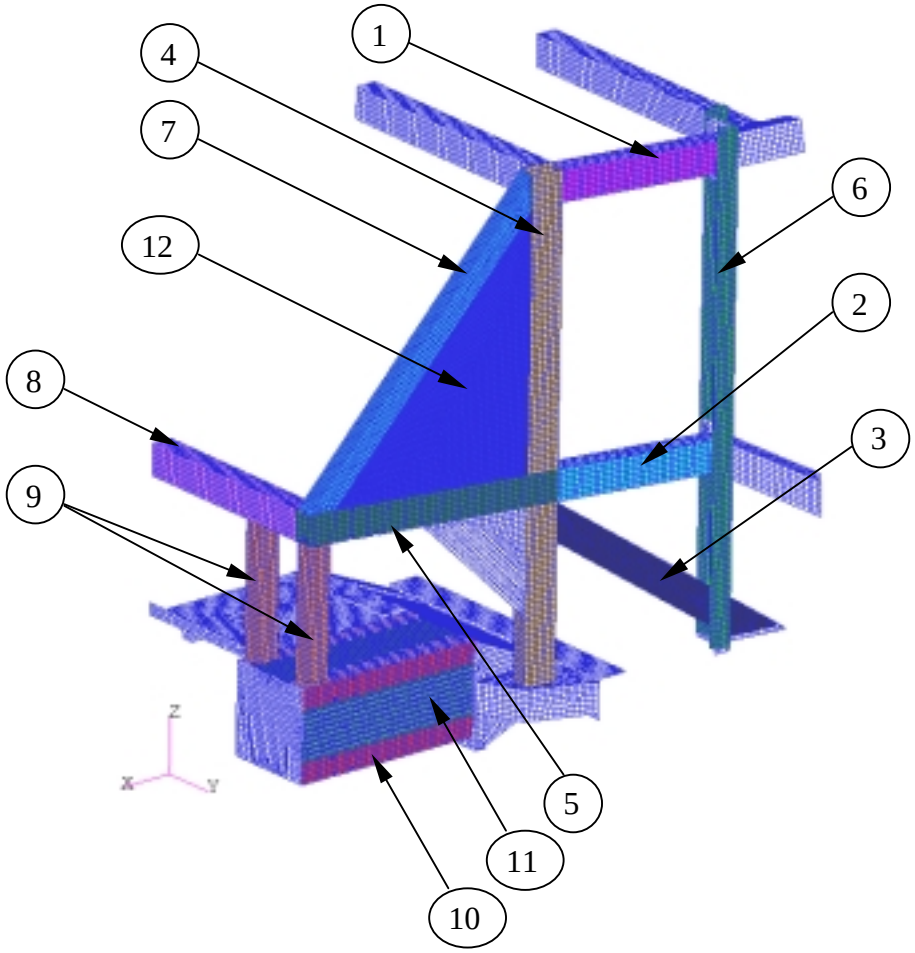

Fig. 8. The design variables that were chosen to be optimized and the global coordinate system.

For denomination of each design variable, in the current study together with initial thickness and mass, se table 1.

Table 1. The denomination of the design variables and their initial thickness and mass.

Beam:	Design variable denomination:	Initial mass [kg]	Initial thickness [mm]:
1	t_108	9.0	3
2	t_109	11.9	4
3	t_110	22.9	5
4	t_112	42.0	5
5	t_113	23.1	5
6	t_114	49.3	6
7	t_116	14.8	3
8	t_117	11.1	3
9	t_118	11.8	3
10	t_119	34.1 (4)	3
11	t_128	21.3 (4)	1.5
12	t_145	13.4	3

The numbers within the parenthesis only point out the number of parts belonging to the same design variable in the FE-model.

To obtain values for the constraint functions i.e. input data to LS-OPT, a simulation with the initial values of the design variables were performed using LS-DYNA. The intrusions and the accelerations have been measured on a node at the center of each cylinder, see figure 9.

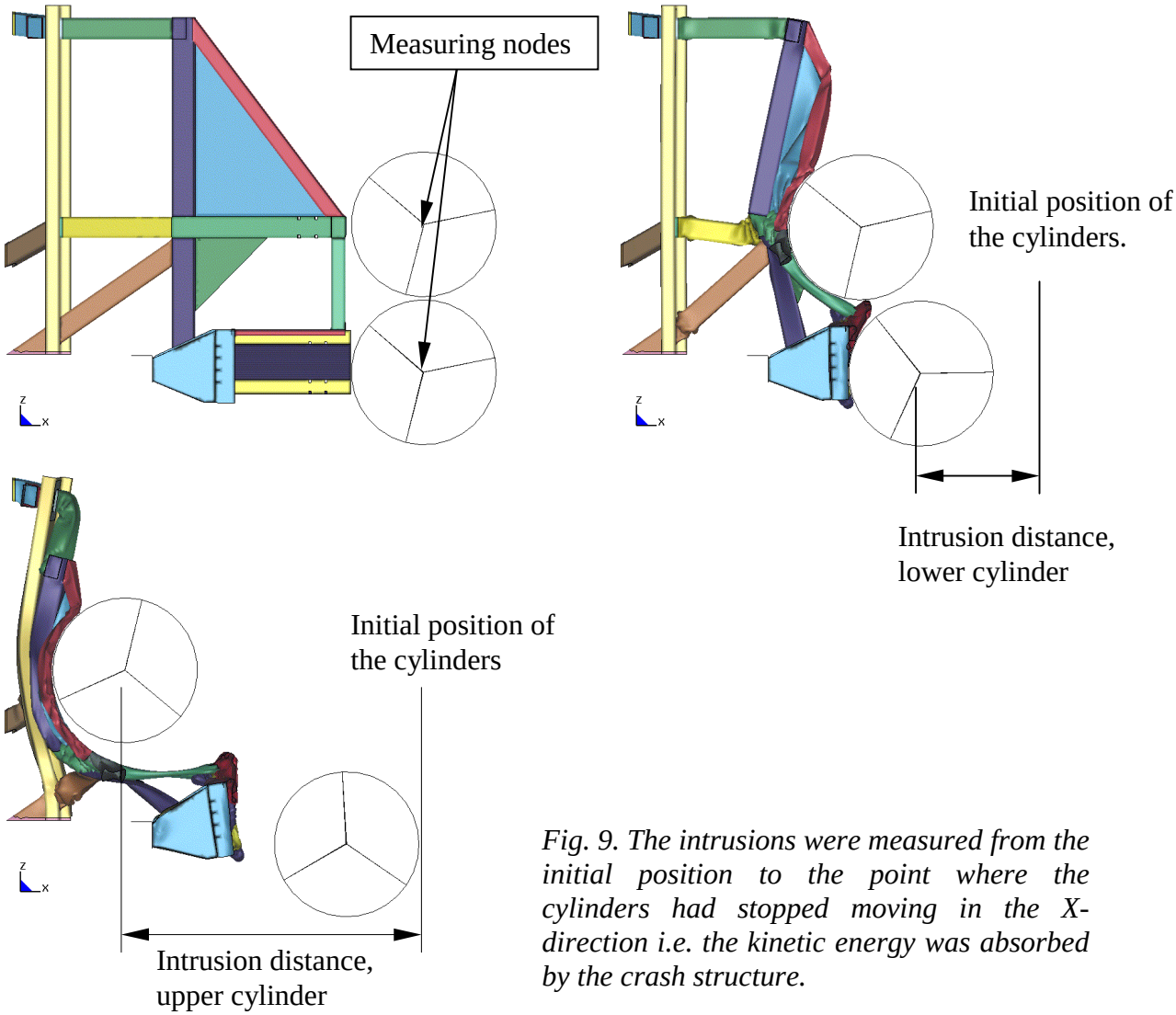

Fig. 9. The intrusions were measured from the initial position to the point where the cylinders had stopped moving in the X-direction i.e. the kinetic energy was absorbed by the crash structure.

From the same LS-DYNA simulation, the time needed to cover the complete crash process was determined to be 148 ms, which was the time used in the optimization setup. A more accurate way to determine the termination time would have been to control the termination time by the kinetic energy of the cylinders, i.e. when the kinetic energy of the cylinders are zero the simulation is stopped. This option was not available in the current version of LS-OPT.

Three approaches were considered regarding how the accelerations were to be defined:

1. ***Unfiltered acceleration curves.*** The all-over maximum value of the acceleration was set as the maximum allowed acceleration on each cylinder according to:

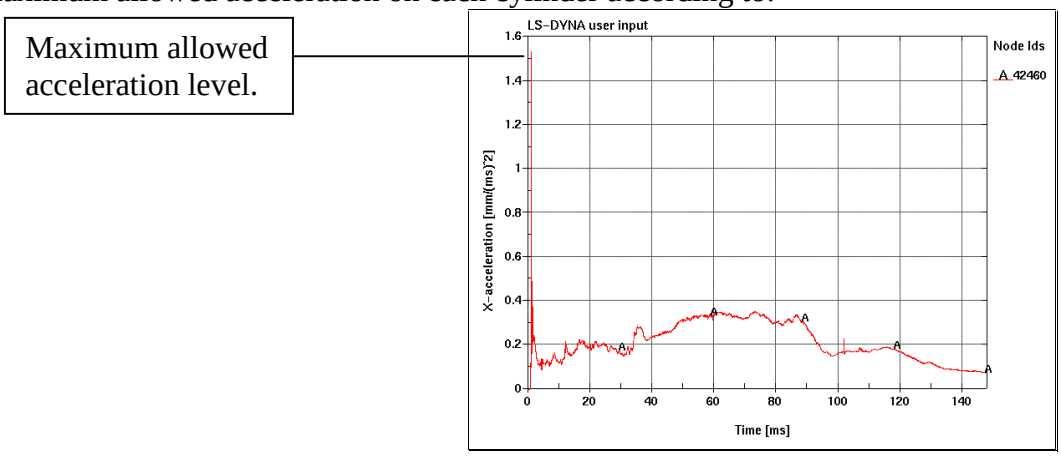

2. ***Filtered acceleration curves.*** The all-over maximum value of the acceleration using a SAE-filter with a frequency of 1000 Hz.was set as the maximum allowed acceleration on each cylinder according to:

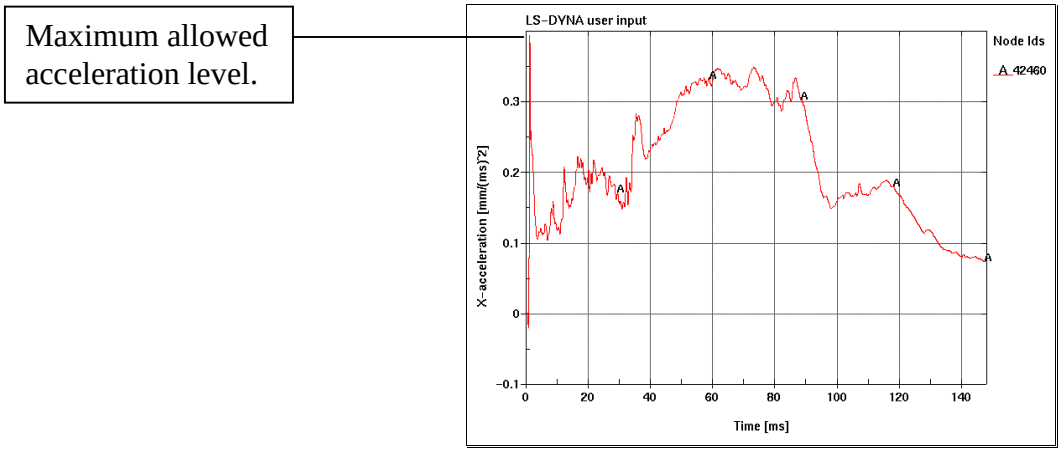

3. ***Mean acceleration.*** The value of the mean acceleration during the whole calculation was set as an upper limit of allowed acceleration level on each cylinder. This can be done in LS-Post by integrating the acceleration curve and then divide the area with the total time for the analysis. However, in the current study, the sum of all acceleration values at each time step were calculated and then divided by the number of time steps and a mean acceleration of the whole crash process could be determined. The upper cylinder affected the structure during the whole crash whereas the mean acceleration of the lower cylinder was computed during the first 50 ms. i.e. the time that the lower cylinder is affecting the crash-structure.

Tables 2 to table 4 show the values obtained from the LS-DYNA simulation that were used as constraint values for the optimization.

Table 2. The value of the constraint used in the optimization. Unfiltered acceleration curves.

Constraints:	**Lower limit:**	**Upper limit:**
Intrusion, Upper cylinder:	-2062 mm.	∞
Intrusion, Lower cylinder:	-817.3 mm	∞
Acceleration, Upper cylinder:	-∞	1.55 mm/(ms)^2
Acceleration, Lower cylinder:	-∞	1.77 mm/(ms)^2

Table 3. The value of the constraint used in the optimization. Filtered acceleration cuves.

Constraints:	**Lower limit:**	**Upper limit:**
Intrusion, Upper cylinder:	-2062 mm.	∞
Intrusion, Lower cylinder:	-817.3 mm	∞
Acceleration, Upper cylinder:	-∞	0.396 mm/(ms)^2
Acceleration, Lower cylinder:	-∞	1.33 mm/(ms)^2

Table 4. The value of the constraint used in the optimization. Mean acceleration.

Constraints:	**Lower limit:**	**Upper limit:**
Intrusion, Upper cylinder:	-2062 mm.	∞
Intrusion, Lower cylinder:	-817.3 mm	∞
Acceleration, Upper cylinder:	-∞	0.211 mm/(ms)^2
Acceleration, Lower cylinder:	-∞	0.654 mm/(ms)^2

Due to the orientation of the global coordinate system, see figure 8, where the cylinders travel in the negative X-direction, the intrusions were defined as the lowest negative value that was allowed.

Moreover, with 12 design variables, this resulted in 20 simulations per iteration. LS-OPT was allowed to perform three iterations per optimization analysis except for the analysis using the mean acceleration as constraint where LS-OPT was allowed to perform five iterations.

5. Results

The objective with the current study was to decrease the mass of the crash-structure without worsen the crash performance with respect to intrusion and acceleration levels. The constraints used were the intrusion of the upper and lower cylinder respectively and the acceleration at a node at the center of each cylinder. Three different approaches were used to define the constraints with respect to acceleration, see section 4.5.2. Therefore, the results are presented with respect to the type of acceleration constraint used.

5.1 Unfiltered acceleration curves

The all-over maximum value of the unfiltered acceleration was set as the maximum allowed acceleration level on each cylinder. Since it is not possible, in the present version of LS-OPT, to get discrete thickness of the design variables, the values of the design variables are presented as they are presented in LS-OPT.

The change of the total mass of the chosen beams during the iterations is shown in figure 10. Whether/ the acceleration and intrusion fulfill the constraints or not is shown in figure 11 and figure 12. The intrusions are presented as the absolute value of the intrusions i.e. they are defined as positive in the following figures.

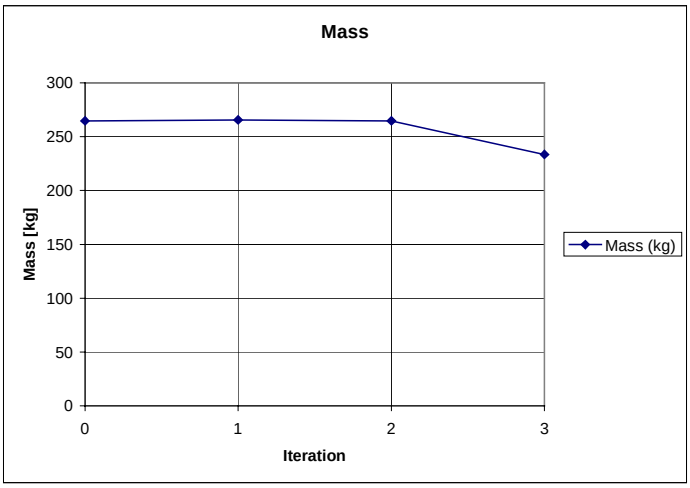

Fig. 10. The change in mass during the analysis using unfiltered acceleration curves.

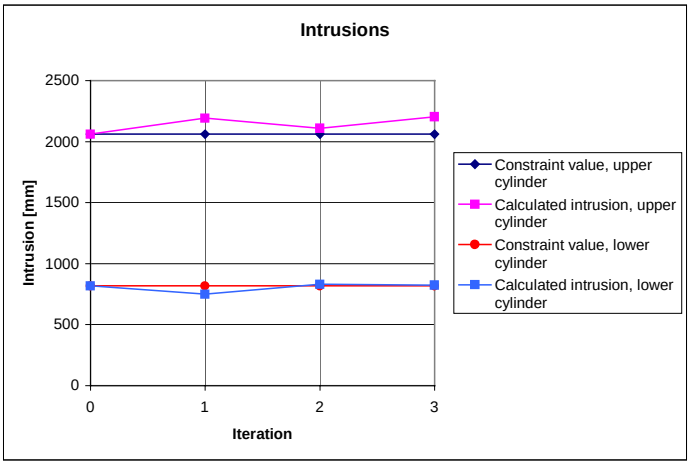

Fig. 11. Calculated intrusions vs. the constraint values using unfiltered acceleration curves.

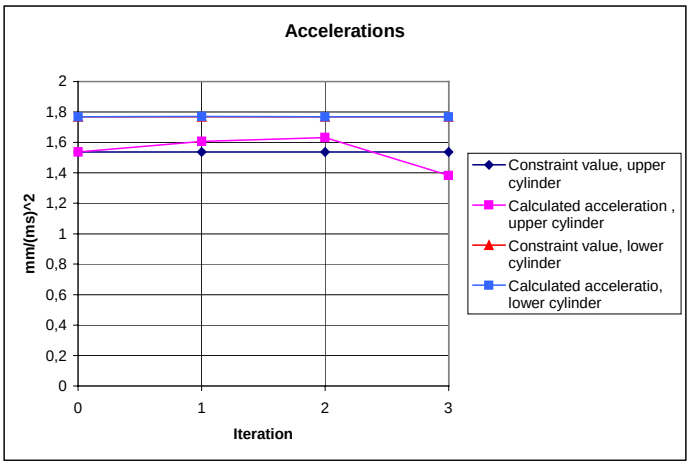

Fig. 12. Calculated accelerations vs. the constraint values using unfiltered acceleration curves.

As can be seen in figure 10, the mass does not change very much in iteration 1 and 2 while in iteration 3, the mass is reduced drastically. However, studying figure 11, it shows that the intrusion of the upper cylinder has been exceeded in all iterations. The intrusion of the lower cylinder was within the constraint value in iteration 1 and in iteration 2 and 3 it is very close to the constraint value.

The acceleration of the lower cylinder is very close to the constraint value. For the upper cylinder, the constraint value is exceeded in the first two iterations and well below the constraint value in the third iteration. The results after the optimization are summarized in table 5.

Table 5. The results from the optimization using unfiltered acceleration curves.

	Before optimization:	After optimization:	Deviation (%):
Mass of design variables (kg):	264,7	234,5	-11.4
Intrusion, upper cylinder (mm):	-2062	-2202	+6.8
Intrusion, lower cylinder (mm):	-817	-823	+0.7
Acceleration, upper cylinder (mm/(ms)^2):	1.55	1.38	-11.0
Acceleration, lower cylinder (mm/(ms)^2):	1.77	1.77	0

The mass is reduced but the intrusion of, especially the upper cylinder, is exceeded.

For more information regarding the change of thickness of the design variables, see Appendix A.

A total number of 61 simulations for the whole optimization were performed.

Between four and seven processors were used and the total time for the analysis to be completed was approximately 150 h. real time.

5.2 Filtered acceleration curves

The all-over maximum value of the filtered acceleration was set as the maximum allowed acceleration level on each cylinder. The filter used was a SAE-filter of 1000 Hz. Since it is not possible, in the present version of LS-OPT, to get discrete thickness of the design variables, the values of the design variables are presented as they are presented in LS-OPT.

The change of the total mass of the chosen beams during the iterations is shown in figure 13. Whether the acceleration and intrusion fulfill the constraints or not are shown in figure 14 and figure 15. The intrusions are presented as the absolute value of the intrusions i.e. they are defined as positive in the following figures.

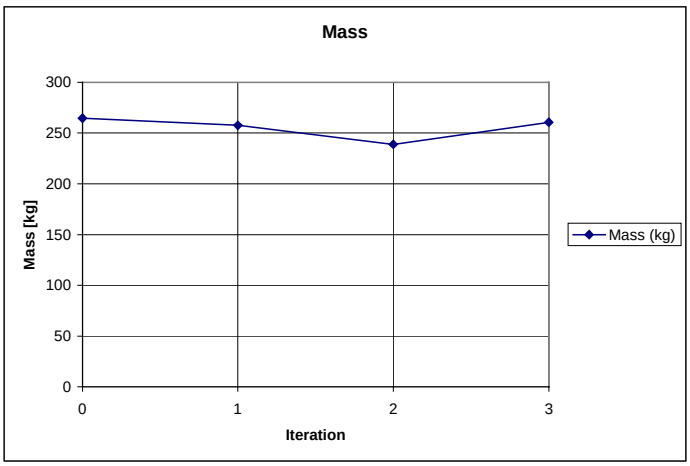

Fig. 13. The change in mass during the analysis using filtered acceleration curves.

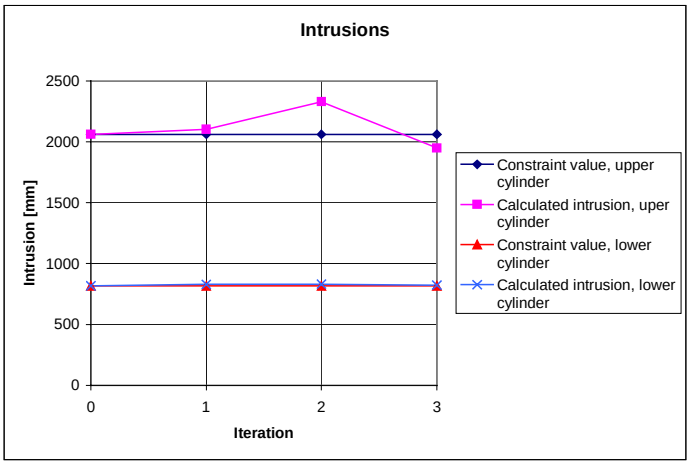

Fig. 14. Calculated intrusions vs. the constraint values using filtered acceleration curves.

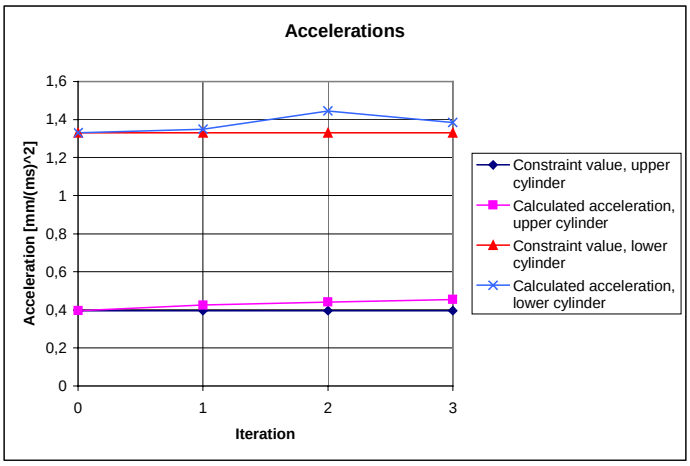

Fig. 15. Calculated accelerations vs. the constraint values using filtered acceleration curves.

The mass is slightly decreased during the first two iterations, see figure 13. In the meantime the intrusion and acceleration of the upper cylinder are exceeded with the maximum violation when the mass is at its lowest value. In iteration three, the intrusion of the lower cylinder is within the constraint limit but the acceleration for both cylinders exceed the constraint value. The results after the optimization are summarized in table 6.

Table 6. The results from the optimization using filtered acceleration curves.

	Before optimization:	After optimization:	Deviation (%):
Mass of design variables (kg):	264.7	260.7	-1.5
Intrusion, upper cylinder (mm):	-2062	-1949	-5.5
Intrusion, lower cylinder (mm):	-817	-823	+0.7
Acceleration, upper cylinder (mm/(ms)^2):	0.396	0.454	+14.6
Acceleration, lower cylinder (mm/(ms)^2):	1.33	1.38	+3.8

The mass is decreased but all constraints are violated except the intrusion of the upper cylinder.

For more information of the change of thickness of the design variables, see Appendix B.

Between four and seven processors were used and the total time for the analysis to complete was approximately 150 h. real time.

5.3 Mean acceleration

The value of the mean accelerations during the whole calculation was set as an upper limit of allowed acceleration level on each cylinder. A total number of five iterations were allowed.

The change of the total mass of the chosen beams during the iterations is shown in figure 16. Whether the acceleration and intrusion fulfill the constraints or not are shown in figure 17 and figure 18. The intrusions are presented as the absolute value of the intrusions, i.e. they are defined as positive in the following figures.

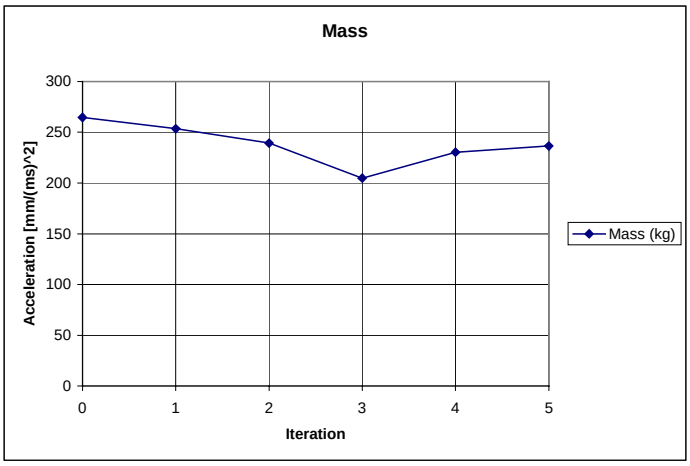

Fig. 16. The change in mass during the analysis using mean accelerations.

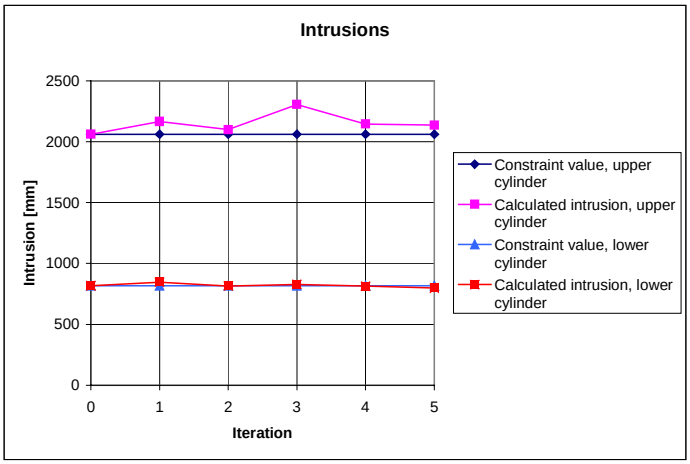

Fig. 17. Calculated intrusions vs. the constraint values using mean accelerations.

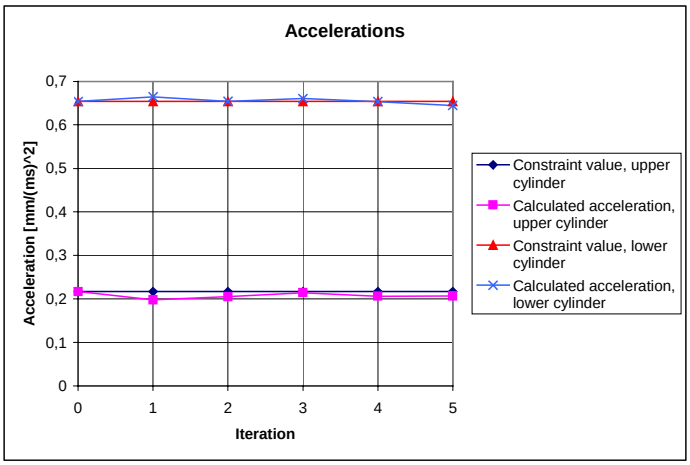

Fig. 18. Calculated accelerations vs. the constraint values using mean accelerations.

The mass is decreased until the fourth iteration where it is increased. The intrusion of the upper cylinder exceeds the constraint but the intrusion of the lower cylinder and the acceleration of both cylinders stay within the constraint value. The results after the optimization are summarized in table 7.

Table 7. The results from the optimization using mean accelerations..

	Before optimization:	After optimization:	Deviation (%):
Mass of design variables (kg):	264.7	236.5	-10.7
Intrusion, upper cylinder (mm):	-2062	-2136	+3,6
Intrusion, lower cylinder (mm):			
Acceleration, upper cylinder (mm/(ms)^2):	0,217	0.207	-4.6
Acceleration, lower cylinder (mm/(ms)^2):	0.654	0.645	-1.4

The mass is decreased by 10.7 % and the only constraint that is violated is the intrusion of the upper cylinder.

For more information of the change of thickness of the design variables, see Appendix C.

Between four and seven processors were used and the total time for the analysis to complete was approximately 250 h. real time.

6. Conclusions

A total satisfactory result was not obtained in the current study since at least one constraint was violated. However, the result from the analyses shows that the weight can be reduced by approximately 54 kg. Considering discrete thickness of the beams, a weight reduction of approximately 40 kg is realistic. Taking into account that the crash-structure already has been manually optimized and that only 12 parts of the crash structure were considered, the result looks very promising.

It has to be remembered that the problem was simplified to decrease the computational time without losing relevance of the purpose i.e. to investigate whether LS-OPT can deal with such a complex process as a crash simulation. Due to these simplifications, the results cannot directly be transformed to the current design but the results give good hints that the weight of the crash structure can be reduced. Despite the simplifications introduced, the study shows that LS-OPT is definitely a useful tool when it comes to crash analyses in future projects.

The study shows that the results of the optimizations depend on how the constraints are defined, in this case the accelerations. How the constraint due to acceleration shall be defined needs further investigations.

The computation time is highly dependent on the number of design variables that are to be optimized and the number of iterations that are to be performed. In the current study 12 design variables were considered. The analyses were run on four to seven processors (depending on the number of available processors) and the total computation time was approximately 150 to 250 h. depending on how many iterations LS-OPT was allowed to perform.

The termination time, i.e. the time when all kinetic energy is supposed to be absorbed, for all simulations was set to 148 ms. However, depending on the design of a specific iteration, the termination time may vary for each iteration. This may result in that the crash structure has 70 not absorbed all the kinetic energy from the cylinders and constraints that were fulfilled would not be fulfilled if the termination time had been longer. A more accurate way to determine the termination time would have been to control the termination time by the kinetic energy of the cylinders, i.e. when the kinetic energy of the cylinders are zero, the simulation is stopped. In the current study however, the differences in result if the termination time would have been longer are considered to be small.

Several problems turned up during the project. Some of the problems resulted in that an ongoing optimization had to be stopped, the problem had to be solved and the current iteration had to be restarted. The presented computation times are therefore estimated. Since one processor is required for each simulation, more processors and LS-DYNA licenses would decrease the computation time. A generalization of how many processors and LS-DYNA licenses that would be suitable to use is impossible to make but having one processor and one LS-DYNA license for each simulation would be the most efficient action to decrease the computation time. This because LS-OPT first has to finish the first iteration before the second iteration is begun. If all simulations within one iteration could be solved directly instead of having simulations in one iteration in queue waiting for an available processor and LS-DYNA license, this would decrease the computation time drastically.

More investigations have to be performed, preferably on smaller models to get faster response, and in this way to learn more about the options available in LS-OPT.

7. References

[1] M. Ristinmaa and C. Ljung. *An Introduction to Stability Analysis*. Lund University, Division of Solid Mechanics.1998.

[2] M. Ristinmaa and N.S. Ottosen. *Large Strain Plasticity*. Lund University, Division of Solid Mechanics. 1996.

[3] M. Ristinmaa and N.S. Ottosen. *The Mechanics of Constitutive Modelling, Volume 1*. Lund University, Division of Solid Mechanics.1999.

[4] K-L. Bathe. *Finite Element Procedures*. John Wiley & Sons Ltd. Northwestern University 1996.

[5] T. Belytschko, W.K. Lui and B. Moran. *Nonlinear Finite Elements for Continua and Structures*. Prentice Hall. Massachusetts Institute of Technology. 2000.

[6] G. Broman. *Computational Engineering*. Blekinge Institute of Technology, Department of Mechanical Engineering. 1999.

[7] M. Ristinmaa and N.S. Ottosen. *The Mechanics of Constitutive Modelling, Volume 2*. Lund University, Division of Solid Mechanics. 1999.

[8] J.O.Hallquist.*LS-DYNA Theoretical Manual*. Livermore Software Technology Corporation. 1998.

[9] J. Forsberg. *Simulation Based Crashworthiness Design-Accuracy Aspects of Structural Optimization using Response Surfaces*. Linköping University, Division of Solid Mechanics. 2002.

[10] N. Stander. *LS-OPT Command Language*. Livermore Software Technology Corporation. 2002.

[11] N. Stander and K. Craig. *LS-OPT User's Manual.* Livermore Software Technology Corporation. 2002.

[12] J.O. Hallquist. *LS-DYNA Keyword User`s Manual*. Livermore Software Technology Corporation. 1998.

[13] J. Borg. *3EST 76-857*. Bombardier Transportation. 1999.

[14] *Technical Specification for Interoperability "Rolling Stock" Sub-system.* Bombardier Transportation. 1999.

8. Appendix

A. Change of design variables using unfiltered acceleration curves.

B. Change of design variables using filtered acceleration curves.

C. Change of design variables using mean accelerations.

Appendix A

Appendix A. The results from the optimization using unfiltered acceleration curves.

Design variable:	Original thickness [mm]:	Optimized thickness [mm]:	Original mass [kg]:	Optimized mass [kg]:	Change of mass [%]:
t_108	3	3.75016	8.997	11.247	+25.008
t_109	4	1.39977	11.88	4.1573	-65.006
t_110	5	6.45043	22.86	29.491	+29.007
t_112	5	6.06745	42.04	51.015	+21.349
t_113	5	3.31793	23.10	15.329	-33.641
t_114	6	2.09974	49.29	17.249	-65.005
t_116	3	3.75016	14.84	18.551	+25.007
t_117	3	2.38651	11.12	8.8460	-20.45
t_118	3	3.75024	11.78	14.726	+25.008
t_119	3	2.75484	34.14	31.350	-8.172
t_128	1.5	1.58407	21.29	22.483	+5.604
t_145	3	2.24986	13.39	10.042	-25.004

Appendix B

Appendix B. The results from the optimization using filtered acceleration curves.

Design variable:	Original thickness [mm]:	Optimized thickness [mm]:	Original mass [kg]:	Optimized mass [kg]:	Change of mass [%]:
t_108	3	4.95	8.997	14.845	+64.999
t_109	4	6.35045	11.88	18.861	+58.763
t_110	5	5.85	22.86	26.746	+16.999
t_112	5	5.85	42.04	49.187	+17.000
t_113	5	5.52833	23.10	25.541	+10.567
t_114	6	3.11557	49.29	25.594	-48.075
t_116	3	3.29814	14.84	16.315	+9.939
t_117	3	3.51	11.12	13.01	+16.996
t_118	3	1.81926	11.78	7.1436	-39.358
t_119	3	2.94939	34.14	33.564	-1.687
t_128	1.5	1.584	21.29	22.482	+5.599
t_145	3	1.97018	13.39	8.7936	-34.327

Appendix C

Appendix C. The results from the optimization using mean accelerations.

Design variable:	**Original thickness [mm]:**	**Optimized thickness [mm]:**	**Original mass [kg]:**	**Optimized mass [kg]:**	**Change of mass [%]:**
t_108	3	3.80549	8.997	11.413	+26.9
t_109	4	4.09088	11.88	12.150	+2.2
t_110	5	4.91431	22.86	22.468	-1.7
t_112	5	4.90304	42.04	41.225	-2.0
t_113	5	4.14044	23.10	19.129	-17.2
t_114	6	4.03176	49.29	33.121	-32.8
t_116	3	4.32991	14.84	21.419	+44.3
t_117	3	1.24166	11.12	4.6024	-58.6
t_118	3	1.73143	11.78	6.7987	-42.3
t_119	3	3.36372	34.14	38.279	+12.1
t_128	1.5	0.97395	21.29	13.824	-35.1
t_145	3	2.99569	13.39	13.371	-0.1